This is a preprint, the final version is subject to change, of the American Mineralogist (MSA)
Cite as Authors (Year) Title. American Mineralogist, in press.
(DOI will not work until issue is live.) DOI: http://dx.doi.org/10.2138/am-2016-5738CCBY

Revision 1

Multi-scale 3-dimensional characterisation of iron particles in dusty olivine: implications for paleomagnetism of chondritic meteorites

Joshua F. Einsle[1,2], Richard J. Harrison[1], Takeshi Kasama[3], Pádraig Ó Conbhuí [4], Karl Fabian[5], Wyn Williams[4] Leonie Woodland[7], Roger R. Fu[8], Benjamin P. Weiss[9], Paul A. Midgley[2]

AFFILIATIONS

1. Department of Earth Sciences, University of Cambridge, Downing Street, Cambridge CB2 3EQ, U.K.
2. Department of Materials Science & Metallurgy , University of Cambridge , 27 Charles Babbage Road, Cambridge CB3 0FS, UK.
3. Center for Electron Nanoscopy, Technical University of Denmark, Kongens Lyngby, Denmark
4. Grant Institute of Earth Science, University of Edinburgh, Kings Buildings, West Mains Road, Edinburgh, EH93JW, United Kingdom
5. Geological Survey of Norway, Leiv Eirikssons vei 39, 7491 Trondheim, Norway
6. CAGE - Centre for Arctic Gas Hydrate, Environment and Climate; Department of Geology, University of Tromsø, NO-9037 Tromsø, Norway
7. The Stephen Perse Foundation, Union Road, Cambridge, CB2 1HF, UK

8. Lamont-Doherty Earth Observatory, Columbia University, Palisades, NY, USA.
9. Department of Earth, Atmospheric and Planetary Sciences, Massachusetts Institute of Technology, Cambridge, MA, USA.

Abstract

Dusty olivine (olivine containing multiple sub-micrometer inclusions of metallic iron) in chondritic meteorites is considered an ideal carrier of paleomagnetic remanence, capable of maintaining a faithful record of pre-accretionary magnetization acquired during chondrule formation. Here we show how the magnetic architecture of a single dusty olivine grain from the Semarkona LL3.0 ordinary chondrite meteorite can be fully characterised in three dimensions, using a combination of Focussed-Ion-Beam nanotomography (FIB-nT), electron tomography and finite-element micromagnetic modelling. We present a three-dimensional (3D) volume reconstruction of a dusty olivine grain, obtained by selective milling through a region of interest in a series of sequential 20 nm slices, which are then imaged using scanning electron microscopy. The data provide a quantitative description of the iron particle ensemble, including the distribution of particle sizes, shapes, interparticle spacings and orientations. Iron particles are predominantly oblate ellipsoids with average radii 242 ± 94 nm by 199 ± 80 nm by 123 ± 58 nm. Using analytical TEM we observe that the particles nucleate on sub-grain boundaries and are loosely arranged in a series of sheets parallel to (001) of the olivine host. This is in agreement with the orientation data collected using the FIB-nT, and highlights how the underlying texture of the dusty olivine is crystallographically constrained by the olivine host. The shortest dimension of the particles is oriented normal to the sheets and their longest dimension is preferentially aligned within the sheets.

Individual particle geometries are converted to a finite-element mesh and used to perform micromagnetic simulations. The majority of particles adopt a single vortex state, with 'bulk' spins that rotate around a central vortex core. We observed no particles, which are in a true single domain state. The results of the micromagnetic simulations challenge some pre-conceived ideas about the remanence carrying properties of vortex states. There is often not a simple predictive relationship between the major, intermediate and minor axes of the particles and the remanence vector imparted in different fields. Although the orientation of the vortex core is determined largely by the ellipsoidal geometry (i.e., parallel to the major axis for prolate ellipsoids and parallel to the minor axis for oblate ellipsoids), the core and remanence vectors can sometimes lie at very large (tens of degree) angles to the principal axes. The subtle details of the morphology can control the overall remanence state, leading in some cases to a dominant contribution from the bulk spins to the net remanence, with profound implications for predicting the anisotropy of the sample. The particles have very high switching fields (several hundred mT), demonstrating their high stability and suitability for paleointensity studies.

1. Introduction

Chondritic meteorites have a long and complex formation history, involving condensation of primary minerals from the solar nebula, high-temperature processing during chondrule-forming events within the protoplanetary disk, accretion followed by thermal and/or aqueous metamorphism on the parent body, exposure to impact-related shocks, heating during passage through the Earth's atmosphere, weathering at the Earth's surface and hand magnet remagnetization during collection and curation (Weiss et al.

2010). This complexity makes chondritic meteorites particularly challenging from a paleomagnetic perspective. Chondrites are magnetically heterogeneous on multiple length scales ranging from metres to nanometres. Spatial variations in remanent magnetization result from the presence or absence of magnetic fields at different stages of their formation history. The challenge for paleomagnetists is to deconvolve the various components of remanent magnetization, and determine the intensity and origin of the magnetising fields.

Recent progress in this area has been driven by the development of scanning SQUID microscopy (Weiss et al. 2007), which enables the remanent magnetic field of a polished thin section to be measured with spatial resolution ~100 μm. Using a SQUID microscope, combined with a non-magnetic microdrill, remanence measurements can be made on mutually oriented sub-samples that are just a few tens of micrometres in size. By focussing on these microscale regions of interest (MROI), the spatial heterogeneity of magnetic remanence can be directly addressed and regions containing the most reliable magnetic remanence carriers can be targeted for study. Although this approach offers the only practical route to obtaining reliable paleomagnetic information from chondrites, it comes at a high price: the smaller the volume of sample studied, the more its paleomagnetic signal becomes dominated by the specific characteristics of remanence carriers contained within it. For example, measurements made on a single silicate grain are sensitive to the local anisotropic arrangement of remanence carriers, whereas such local effects are averaged out in a bulk measurement. Interpreting paleomagnetic results with confidence, therefore, requires a full three-dimensional characterisation of the internal magnetic architecture of the MROI.

Here we describe how this goal can be achieved by using a Dual Beam Focused Ion Beam – Scanning Electron Microscope (FIB-SEM) to perform FIB-nanotomography (FIB-nT). The tomographic technique involves sequentially cross-sectioning through a selected MROI using the FIB and then imaging each cross-sectional face with the SEM (Holzer et al. 2004; De Winter et al. 2009; Schiffbauer and Xiao 2009; Bera et al. 2011; Keller et al. 2011a, 2011b; Holzer and Cantoni 2012; Landrot et al. 2012; Kruhl et al. 2013). The stack of high-resolution SEM images are then reassembled into a three dimensional (3D) volume, which is analysed quantitatively to extract the physical properties of the ensemble of particles. The 3D information is then used as the input to micromagnetic simulations that enable the magnetic properties of both individual particles and (in principle) the ensemble as a whole to be calculated.

We apply this method to a sample of 'dusty olivine' extracted from chondrules in the Semarkona LL3.0 ordinary chondrite, which recently formed part of a study to measure the strength of the magnetic field present during chondrule formation (Fu et al. 2014). The term 'dusty olivine' refers to grains of olivine containing numerous sub-micron inclusions of metallic Fe. Dusty olivines are thought to be relic grains of olivine that were caught up in a chondrule-forming event, heated (without melting) under reducing conditions to temperatures above the Curie temperature of the Fe inclusions, and then cooled in the presence of the nebular magnetic field (Connolly et al. 1998; Leroux et al. 2003; Hewins et al. 2005; Uehara and Nakamura 2006). Recent studies of synthetic analogues of dusty olivine, created by laboratory reduction of terrestrial olivine precursors, suggest that this material has the potential to maintain a faithful record of pre-accretionary remanence (Uehara and Nakamura 2006; Lappe et al. 2011, 2013).

114 However, these conclusions were primarily based on transmission electron microscopy
115 (TEM) measurements of individual Fe particles in laboratory analogues (Lappe et al.
116 2011). TEM analysis requires thinning a sample to a foil less than 200 nm thick, thereby
117 obscuring the original size, shape and spatial distribution of the magnetic remanence
118 carriers. The approach put forward here, in contrast, preserves precisely the 3D
119 information needed to reconstruct the magnetic architecture of the MROI. Furthermore,
120 we apply this technique directly to natural dusty olivine samples.

121 ## 2. Experimental Methods

122 ### 2.1 Sample

123 The sample is a grain of dusty olivine extracted from a chondrule of the
124 Semarkona LL3.0 chondrite (sample DOC5 from Fu et al. 2014). A full description of all
125 sample preparation steps performed prior to our study is given by Fu et al. (2014). The
126 sample was mounted on a quartz disk stub with epoxy, and the magnetic reference axes
127 of the grain were marked. This enables the extraction of nanoscale information to be
128 correlated back to the macroscopic magnetic measurements made by Fu et al. (2014).
129 After optical investigation, the quartz disc was mounted onto a 38 mm SEM stub and
130 carbon coated. Much of the sample surface was initially obscured by epoxy (Fig. 1a).
131 Small bright specks visible in the exposed region of the grain correspond to the metallic
132 Fe particles that define dusty olivine. FIB-nT was performed on the region highlighted in
133 Fig 1a. The chosen region was adjacent to the region where a TEM lamella had
134 previously been extracted from the olivine grain (Fu et al. 2014). The same TEM lamella
135 was used to perform the additional TEM measurements reported here. The imaging

surfaces for both FIB-nT and TEM studies were acquired parallel to each other, allowing us to make direct comparisons across the length scales captured.

2.2 FIB-nT

FIB-nT was performed using a FEI Helios Nanolab Dual Beam microscope at the University of Cambridge. The sequential slicing and imaging sequence was controlled by the Auto Slice and View G3 (ASVG3) application. All FIB milling was performed using an accelerating voltage of 30 kV. The MROI was prepared by depositing a protective 10 μm by 15 μm by 1 μm tungsten pad using ion beam induced deposition with an ion beam current of 3 nA. The MROI was isolated from the bulk sample by selectively milling 20 μm deep trenches on three sides of the region defined by the W pad (Figs. 1b – d) using a 7 nA ion beam current. The front trench allows full viewing access to the cross sectional surface and the side trenches minimize re-deposition effects associated with the sequential sectioning process. Figure 1b shows the tomographic region of interest immediately after clearing away excess material. Finally, a pair of fiducial marks was created before starting the automated sequence, using the 3 nA ion aperture for W deposition and 300 pA aperture for feature milling. Figure 1c is a FIB micrograph used for slice placement, showing the actual field of view used, taken at an arbitrary point in the automated slice-and-view routine. The fiducial mark seen in Figs. 1b and 1c controls the placement of each slice of the tomographic sequence, whereas the fiducial mark seen in Fig. 1d minimizes the amount of image drift in the SEM image stack. Each 20 nm thick tomographic slice was milled away using a 920 pA ion beam current. All milling was performed at 52° stage tilt, which is normal to the FIB.

Each image of the tomographic sequence was recorded using a dwell time of 20 µs with an 8 bit grey scale and a scan area of 1024 by 884 pixels. The horizontal field width of the final image was set to 10 µm. This gave a final pixel size of 9.766 nm. Imaging of the cross-sectional cut face was achieved using back-scattered electron (BSE) imaging with the SEM operating in immersion mode at a low accelerating voltage of 2 kV with a beam current of 86 pA. We used the through the lens detector in back-scattered electron mode for the strong material contrast mechanism between the olivine host matrix (dark grey) and the Fe nanoparticles (bright greys) (Fig 2a). This combination of through lens detection and backscatter mode also eliminates contrast artefacts like shadowing and allows for higher spatial resolution over Everhart-Thornley detector geometries. SEM imaging conditions were further optimized to reduce noise in the BSE image as well as to ensure that only the cross-sectioned surface was imaged. Reduction of the electron interaction volume was achieved by using the low accelerating voltage of 2 kV. Detector noise in the image was minimised by reducing the working distance from 4 mm to 3.3 mm. Additionally, to protect the pole piece at the shorter working distance the sample was tilted to 47.8°. Movement between the SEM imaging position and the FIB patterning position was controlled automatically through ASVG3. Using this automation routine, 262 slices were recorded over 15.3 hours, with a specified slice thickness of 20 nm resulting in a total milled thickness of 5.2 µm.

2.3 Image Post-Processing

Data post-processing and analysis were performed using a combination of the commercial package ORS Visual SI and the open-source platform FIJI, based on the

ImageJ image analysis distribution (Schindelin et al. 2012). The 262 images were loaded as a single three-dimensional image stack into ORS Visual SI. The pixel aspect ratio was adjusted to correct for the sample tilt and the slice thickness of 20 nm was applied to the image stack. This resulted in voxel dimensions of 9.8 nm by 13.2 nm by 20 nm. Although the fiducial mark seen in Fig. 1b helps to minimize image stack drift, erosion of this feature during the sequential milling of the MROI resulted in a progressive drift in the final image position on the cut face. Applying the Normalized Mutual Information alignment algorithm within ORS Visual SI the image stack alignment tool allowed for precise and jitter-free alignment of the reconstructed volume.

The image stack was segmented to define the Fe particles and olivine matrix (Fig. 2a). Several approaches for this have been documented in the literature (Holzer et al. 2004; Bushby et al. 2011; Keller et al. 2011a). We found that the best results were obtained using simple greyscale thresholding followed by noise reduction and manual artefact removal. Middle grey levels (114 – 212) associated with Fe particles were assigned a saturating value of 255. All other pixels were set to 0. After applying this binary segmentation, residual detector noise was eliminated by one pass of the FIJI/ImageJ despeckle filter. Next, residual W deposition, milling curtain artefacts and particles partially lying on the edges of the reconstructed volume were manually removed from the image stack. Close inspection of the original images revealed saturated black and saturated white pixels around some Fe particles. It is thought that these are pockets of silica glass formed as a by-product of the solid-state reduction reaction that created the Fe particles (Leroux et al. 2003). As these regions are non-conductive, they tend to induce charging effects in the images registering as saturated white. Related to these are

saturated black voxels that upon inspection of the original image stack can be seen to be either non-charging glass (which charge up in subsequent images) or holes in the olivine crystal. The holes and charging artefacts can be seen in Fig. 2a. Grey scale binary segmentation does not fully isolate the Fe particles from these parasitic features and so these regions were manually removed from the segmented images. Fig. 2b shows the same image after binary segmentation and manual artefact removal.

Quantitative three-dimensional analysis of the resulting scaled aligned and segmented image stack was performed using the ImageJ/FIJI plug-in BoneJ version 1.3.15 (Doube et al. 2010; Carriero et al. 2014). The BoneJ Particle Analyser generates a surface mesh for each particle and determines a best-fitting ellipsoid to that surface. Errors in the ellipsoid fitting are of the order of the voxel size and therefore can become significant for particles that are defined by a small number of voxels. Additionally non-physical results were obtained for groups of voxels that appeared only on one image of the stack. These voxel groups consisted of either segmentation noise that was not fully removed, or very small particles with radii less than 20 nm in one dimension (i.e., these are particles that are less than the thickness of a tomography slice). This establishes our 3D resolution limits and means we do not observe any particles with a diameter of less than 40 nm. However, TEM studies did not reveal any particles smaller than this. After artefact removal we were left with 246 particles in the 710 μm3 volume analysed by FIB-nT.

2.4 TEM

To complement the mesoscale tomographic information provided by FIB-nT, we also performed high-resolution TEM studies of individual particles using scanning

transmission electron microscopy (STEM). The TEM lamella was fabricated using FIB milling (Fu et al. 2014). All studies were performed at the Technical University of Denmark (DTU) on an FEI Titan 80-300 TEM equipped with a field-emission electron source, monochromator, spherical aberration probe corrector, Lorentz lens and electrostatic biprism. All measurements were made using 300 kV accelerating voltage. Preliminary Lorentz microscopy and electron holography observations were reported by Fu et al. (2014).

Here we present bright-field TEM and STEM imaging, electron diffraction data as well as dark-field STEM tomography results. Both TEM and bright-field STEM modes allow us to image crystallographic features such as dislocations and sub-grain boundaries (Williams and Carter 2002; Crewe and Nellist 2009). Dark-field STEM tomography of a single particle was performed using a camera length of 130 mm to produce a strong material contrast between the Fe particles and the olivine crystal. The tomographic series was collected at a magnification of 28500X (giving a pixel size of 3.26 nm) using the high angle annular dark field (HAADF) detector. The tilt series consisted of an image taken every 2° for tilts from -76° to +76°. Alignment and reconstruction of the tilt series was achieved using Inspect 3D with the SIRT algorithm (Gilbert 1972). Visualisation was performed using Avizo Fire.

2.5 Micromagnetic Modelling

A selection of Fe metal particles, representing the range of sizes and shapes within the ensemble, were chosen to perform detailed micromagnetic simulations. Each particle was cropped from the segmented FIB-nT stack and converted to a tetrahedral

finite-element mesh in a multi-step process. An example of the initial geometry of a particle defined by the FIB-nT is shown in Fig. 3a. Each rectangular block represents a single 9.8 x13.2 x 20 nm voxel. This representation of the particle was used to generate a bounding polyhedron that best approximates the actual particle surface, where each point of the resulting mesh must solve a Poisson boundary condition (Fig 3b). We further refine the surface mesh by passing it through a surface smoothing routine (Fig. 3c). We coarsen the smoothed surface using a Delaunay triangulation routine to produce a surface mesh at the desired resolution of 5 nm (Fig. 3d). The final triangular surface mesh was imported into the software package CuBit (KitWare), where it was turned into a tetrahedral volume mesh. We used an initial surface mesh with average node spacing 5 nm, which was then used to generate tetrahedral nodes on average every 5 nm throughout the volume. Although this resulted in a mesh size slightly bigger than the 3.4 nm exchange length for iron, it enabled the number of elements in the model to be kept below approximately 300,000 and provides acceptable resolution for modelling simple vortex micromagnetic structures.

Micromagnetic modeling was performed using MERRILL (Micromagnetic Earth Related Rapid Interpreted Language Laboratory), a micromagnetics package optimized for the rock magnetic community developed by K. Fabian and W. Williams (Williams and Fabian 2016). MERRILL uses a Finite Element Method/Boundary Element Method (FEM-BEM) to solve for the magnetic scalar potential inside the particle and thereby calculate the demagnetizing energy of the system. The use of FEM-BEM avoids the need to discretize the non-magnetic volume outside the particle. Simulations were performed by minimizing the total micromagnetic energy. This consists of summing the exchange,

cubic anisotropy, magnetostatic and demagnetizing energies. Energy minimization was performed using a conjugate gradient method, specially adapted to micromagnetic problems. MERRILL has been successfully tested against µMAG Standard Problem #3 (http://www.ctcms.nist.gov/~rdm/mumag.org.html).

Material parameters used were appropriate for pure iron at room temperature: saturation magnetization M_s = 1715 kA/m, exchange constant A = 2 x 10^{-11} J/m, and cubic anisotropy with K_1 = 48 kJ/m^3 (Muxworthy and Williams 2015). We arbitrarily set the cubic <100> axes parallel to the X, Y and Z axes of the volume reconstruction. We will show in Section 3.3 that this does not greatly influence our analysis, as the magnetic behavior of the particles studied is dominated by shape rather than magnetocrystalline anisotropy.

Using the method of Hubert (1967), it can be estimated that magnetostrictive effects become important for iron only when the magnetostrictive energy density 9/2 (c_{11}-c_{12}) λ_{100}^2 is of similar size as the energy density ~2(A K_1)$^{1/2}$ /d generated by a 180°-domain wall, where d is the dimension of the particle (Hubert 1967; Fabian et al. 1996; Hubert and Schäfer 1998). For iron with elastic constants c_{11}=241 GPa, c_{12}=146 GPa (Lee 1955), and λ_{100}=22 x10^{-6} (Radeloff 1964), this occurs only for d >9 µm such that magnetostriction can safely be neglected for all modeled particles. Also magnetoelastic interaction is neglected because it is assumed that any strain involved in the formation of the particles has been relaxed by plastic deformation such that no noticeable internal stress field is present.

Simulations were performed using an Apple iMac with a 3.4 GHz Intel i7 processor and 24 GB of RAM. Each particle was initialised with uniform magnetization

297 along either the X, Y and Z axes of the reconstructed volume. Fields varying from 1000
298 mT to -1000 mT in steps of 10 mT were applied along X, Y and Z. The converged set of
299 magnetic moments obtained after each field step was subjected to small random rotations
300 (maximum angle 20°) and then used as the basis for the starting condition for the next
301 field step. This step is to insure that the energy minimisation is not trapped in a local
302 energy minima. The average magnetization projected on each of the X, Y, and Z axes
303 were calculated at each step in order to generate the upper branch of the hysteresis loop.
304 Lower branches were not calculated directly using micromagnetics, but are presented for
305 visualisation purposes under the assumption that these are symmetrically equivalent to
306 the upper branch.

307 ## 3. Results

308 ### 3.1 FIB-nT

309 The reconstructed dusty olivine volume is shown in Fig 4a-c. A qualitative
310 analysis (see movie in supplemental information) reveals that i) the particles are loosely
311 arranged in planar sheets, ii) the particles tend to be flattened in the direction
312 perpendicular to the sheets, and iii) there is a preferred orientation of particle elongation
313 along a direction within the sheets. We will present the crystallographic analysis in
314 section 3.2 when we present the TEM and STEM results. Particles are widely distributed
315 in terms of their size and aspect ratio. Figure 5 summarises this distribution by plotting a
316 histogram of the best-fit ellipsoid diameters for the major (Fig. 5a), intermediate (Fig. 5b)
317 and minor (Fig. 5c) axes. The average particle radii are 242 ± 94 nm by 199 ± 80 nm by
318 123 ± 58 nm. In order to classify the particles in terms of their tendency towards either

uniaxial prolate or uniaxial oblate symmetry, we plot the aspect ratio of the major to intermediate radii against the aspect ratio of the intermediate to minor radii in Fig. 6a (Flinn 1962). This 'Flinn' plot also scales the size of each data point to the size of the major radius. The line $y = x$ separates prolate particles (above the line) from oblate particles (below the line). There are significant populations of small, flattened particles that plot close to the horizontal (uniaxial oblate) and elongated particles that plot close to the vertical (uniaxial prolate) axes. As seen qualitatively in the Flinn plot and quantitatively in the histogram in Fig. 6b, 95% of the particles are classified as oblate in aspect ratio with a mean Flinn ratio of 0.76. This gives the majority of particles a tri-axial symmetry. This non-spherical and non-uniaxial aspect ratio has profound implications for the magnetic anisotropy of each particle, which we will explore in more detail using FEM models (Section 4.3). Of the reconstructed particles, only 11 possess a prolate aspect ratio. The three smallest of these are close to the limitations of our reconstruction resolution. For these particles, the radii are between 2 to 6 voxels long in any one direction, which means that the uncertainty in the ellipsoid-fitting algorithm can be on the order of the size of the particle. We found that extracting these individual particles from the larger tomographic volume and rerunning the BoneJ analysis lead to small changes in the fitted ellipsoid parameters, causing them to be reclassified as oblate. Reported population statistics refer to the results of the whole ensemble fitting, which are accurate for all but these very small particles.

The orientations of major, intermediate and minor ellipsoid axes are shown in Fig. 7. All three axes show pronounced clustering of their principal axes, confirming the qualitative assessment above (note that the ellipsoid fitting does not distinguish between

positive and negative vectors). The minor ellipsoid axes (blue circles) are tightly clustered in the direction normal to the sheets, whereas there is a much broader spread of major and intermediate axes within the sheets (red and green circles, respectively). Solid triangles in Fig. 7 show the principal axes of the anisotropy of susceptibility of anhysteretic remanent magnetization (ARM) for the whole dusty olivine chondrule, as determined by scanning SQUID microscopy (Fu et al. 2014). The coordinate system used for reporting results is based around the orientations of the FIB-SEM microscope. We have transformed the coordinates Fu et. al. (2014) to agree with the microscope system. The average orientation of the major ellipsoid axes coincides with the direction of highest ARM susceptibility, whereas the intermediate and minor susceptibilities lie at angles of ~40° from the average orientations of the intermediate and minor ellipsoid axes, respectively.

3.2 TEM and STEM analysis

Fig. 8a shows a bright-field STEM mosaic of the entire lamella. The prominent dark feature running horizontally along the top of the image is the remains of the Pt capping layer that was deposited on the surface of the sample to protect it during FIB milling. The Pt layer became partially detached from the surface after the lamella was plasma cleaned prior to insertion in the TEM. The Fe particles appear dark against the mid grey olivine background. Silica glass regions appear as light grey blebs parasitic to the Fe particles. Electron diffraction patterns were obtained for the olivine and Fe particles inside the red-boxed region shown in Fig. 8a. Figure 8b has been oriented with respect to the region highlighted in larger montage image. The upper right hand

365 diffraction pattern in Fig 8b was collected from olivine in this region with an α-tilt of -
366 3.5° and a β-tilt of -1.1°, and corresponds to a [130] zone axis (~9° from [010]). The
367 diffraction pattern in the lower left corner of Fig 8b was obtained from the smaller of the
368 two Fe particles with an α-tilt of 8.8° and a β-tilt of -6.8°, and corresponds to a [001]
369 zone axis. The short axis of the particle corresponds to the [100] direction of Fe and lies
370 normal to the (001) plane of olivine. This is in agreement with the orientation data
371 collected using the FIB-nT (inset upper left), and highlights how the underlying texture of
372 the dusty olivine is crystallographically constrained by the olivine host.
373 The lower right hand image in Fig. 8b is a 3D visualisation of the small Fe
374 particle obtained using STEM tomography (Movie of particle in Supplemental
375 Materials). The voxel size is 3.3 nm, at least a factor of 3 smaller than the voxel size
376 obtained via FIB-nT. The particle dimensions are 232 nm by 205 nm by 232 nm (X, Y, Z
377 with respect to the image plane), giving it a slightly oblate profile. These dimensions
378 mean that the particle is one of the smaller ones in the population. It is representative of
379 the largest complete particle that could be imaged using STEM tomography (larger
380 particles were truncated by the surfaces of the TEM foil). Particles of this size (and
381 smaller) are observable using the FIB-nT approach (albeit at considerably lower spatial
382 resolution), so there is some overlap between the size ranges accessible by the two
383 techniques. 2D particle analysis of this lamella does not reveal any particles smaller than
384 those observed in the FIB-nT volume.
385 Figure 8a shows sub-grain boundaries in the olivine running parallel and
386 perpendicular to [001]. As the diffraction pattern for the olivine in Fig 8b is oriented with
387 respect to Fig 8a, we see that the olivine's [001] is perpendicular to the sharp sub-grain

boundaries. In contrast, the sub-grain boundaries running parallel to the [001] are slightly blurred. This broadening we interpret to be the result of the trace of the (010) intersecting the 100 nm thick lamellae surface with an angle of around 9° as noted above. These observations about the arrangement of the sub-grain boundaries are in line with the previous study by Kirby and Wegner (1978), which demonstrated that the dislocation arrays in olivine concentrate along the {100} lattice planes. The dislocations defining the sub-grain boundaries are more clearly visible in the bright-field TEM image (Fig. 8c), which was taken from the region outlined in blue. The sub-grain boundary seen on the right of this image is parallel to (001) of the olivine and lies parallel to a prominent (100) facet of the Fe crystal. This sub-grain boundary is also parallel to the plane containing the major and intermediate axes of the ensemble (inset upper left). Previous studies of natural and synthetic dusty olivines (Leroux et al. 2003; Lappe et al. 2013) have suggested that the Fe nanoparticles arrange along dislocation arrays associated with the sub-grain boundaries. By measuring the crystallographic information of the lamella from the same region, we are able to demonstrate that the particle ensemble does indeed arrange in sheets related to crystallographic planes of the olivine host crystal.

3.3 Micromagnetic Simulations

3.3.1 Remanence states and magnetic moments. The results of micromagnetic simulations for 9 selected particles (8 particles extracted from the FIB-nT stack plus the STEM tomography particle shown in the red inset of Fig. 8) are summarized in Table 1. A range of oblate (Flinn ratio less than 1) and prolate (Flinn ratio greater than 1)

411 ellipsoids are represented, with volumes ranging from the smallest in the ensemble
412 (Particle 48) to those closer to the average (Particle 165). Remanence states were
413 obtained after applying a saturating field of 1 T along the X, Y and Z directions of the
414 reconstructed volume, and then stepping the field down to zero in steps of 10 mT. The
415 squareness M_{rs}/M_s is the magnitude of the total remanence vector normalized to the
416 saturation moment of the particle. To aid comparison and to give a better sense of the
417 magnitude of the magnetic moment of each particle, we define 'relative M_r' as the total
418 remanent moment of the particle divided by the total remanent moment of a uniformly
419 magnetized 25 nm diameter sphere. This size corresponds to the upper threshold for
420 single-domain (SD) Fe (Muxworthy and Williams 2015).
421 No particles were small enough to adopt an SD state. Instead all particles adopt
422 either pseudo-single domain (PSD) or emerging multi-domain (MD) states, consisting of
423 either a single vortex or multiple vortex/wall-like structures (Fig. 9). To highlight the
424 orientation and nature of vortex cores, the magnitude of the vorticity of the moment
425 vector field ($|\nabla \times \boldsymbol{M}|$) is plotted as an isosurface (green in Fig. 9). The choice of
426 isosurface magnitude is somewhat arbitrary (too large and only the ends of the core are
427 highlighted; too small and the surface extends too far from the core region). We chose the
428 largest value that would produce a continuous trace of the core from one surface
429 termination to another. The remanent states of the particles studied can be divided into
430 four general categories: I) single vortex with core oriented close to the minor axis of the
431 best-fitting ellipsoid (Fig. 9a); II) single vortex with core oriented within the plane
432 defined by the minor and major axes of the best-fitting ellipsoid (Fig. 9b); III) single

vortex with core oriented parallel to the major axis of the best-fitting ellipsoid (Fig. 9c); IV) multiple vortex/wall-like structures containing two or more cores (Fig. 9d).

Type I behavior was typically observed in oblate particles with lower Flinn ratios (flattened ellipsoids). Type I particles display straight cores located at the center of the largest face. The relatively strong demagnetizing field of the vortex core in this case can be shielded by antiparallel spin tilting at the outer rim of the oblate particle. Type II behavior was typically observed in oblate particles with higher Flinn ratios (triaxial ellipsoids). Type II particles display curved cores that adopt a sigmoidal trajectory through the center of the particle. The ends of the core lie normal to their surface terminations, as requested by the micromagnetic boundary conditions (e.g., Hubert and Schäfer 1998). Type III behavior was observed in the three prolate particles. Type III particles display cores that track the major ellipsoid axis in the central section of the particle. The ends of cores again lie normal to their surface terminations, causing deviations and distortions of their trajectory. Type IV behavior was observed in the two large prolate particles and already represents a diamond-shape domain pattern with preference for 90° walls, as previously observed for iron thin films and whiskers (e.g., Fig. 5.94 in Hubert and Schäfer, 1998). The remanent state of these particles was more sensitive to the direction of the saturating field than oblate particles with similar volume. In the case of Particle 233 (the largest and most elongated prolate particle), states III, IVa and IVb were adopted for saturating fields applied along X, Y and Z, respectively (Table 1). IVa contains two curved cores corresponding to Bloch walls that split the particle into magnetic domains; IVb is an efficient flux closure structure containing ten magnetic domains (Fig. 9d). □

456 The morphology of the vortex core evolves with increasing volume of particle
457 (Fig. 10). Small particles contain well-defined cylindrical cores (Fig. 10a). Larger
458 particles develop cores with a 'winged' structure, with wings protruding along the
459 directions of emerging domain walls (Fig. 10b). In larger prolate particles, the core is
460 poorly defined, becoming flattened and developing off-shoots (Fig. 10c) and loops (Fig.
461 10d), suggestive of emerging MD behavior.
462 The emerging walls can be better defined and visualized as isosurfaces of the
463 magnetocrystalline anisotropy energy, which highlights those regions where the
464 magnetization points away from the <100> magnetocrystalline easy axes (Fig. 11). As
465 before, the choice of isosurface magnitude is somewhat arbitrary (too large and the
466 domain walls develop holes; too small and the walls become unreasonably wide). We
467 chose a value that generated the thinnest continuous wall structures. Examining the
468 remanent state for each of the orthogonal magnetization directions, a variety of domain
469 wall-like behaviors can be identified. Fig. 11a depicts the Type III remanent state
470 observed after applying saturating fields along X. A cross section through the anisotropy
471 surface of this state is shown in Fig. 11c. The cross section reveals the presence of 4 wall-
472 like structures associated with the rotation of spins around a central vortex core. Due to
473 its alignment with a perpendicular easy axis, the vortex core appears as the cylindrical
474 hole in the center of the anisotropy surface in Fig. 11c. Near the particle center, the
475 domain walls tend to be thinner and better defined. Walls broaden towards the particle
476 surface, as the magnetization adapts to the surface morphology, driven by the need to
477 avoid high magnetostatic energy. Figs. 11b and d show Type IVa and IVb behavior,
478 revealing the presence of well-defined 90° domain walls. Again, there is a tendency for

domain walls to be thinner in the grain interior, broadening and adopting a more Néel-like character as the spins adapt to the surface morphology (Hubert and Rave 1999).

3.3.2 Remanence vectors with respect to particle shape. Stereograms showing the predicted remanence vectors obtained after applying fields along X (black circle), Y (black square) and Z (black triangle) are shown in Fig. 12 for selected particles. Also shown are the orientations of the minor, intermediate and major axes of the best fitting ellipsoids (blue, green and red diamonds, respectively), and the corresponding traces of the planes normal to these directions. For single vortex states, the remanence vector is dictated primarily by the magnetization of the vortex core, but the precise remanence direction is modified significantly by switching the sense of rotation of the bulk spins. Denoting the core direction as either up or down and the sense of bulk spin rotation as being either left or right, this results in two pairs of distinct remanence directions for each particle: (up left and down right) and (up right and down left) (Fig. 12a). The remanence states in each pair are antiparallel to each other, but lie at some angle to the other pair. Remanence directions for two Type I particles are shown in Figs. 12b and 12c. The angle between remanence pairs is 32° for Particle 364 (Fig. 12b) and is 80° for Particle 155 (Fig. 12c). In Particle 364 (a small oblate particle), the remanence lies close to the core direction, i.e. close to the minor axis of the best-fitting ellipsoid (Fig. 12b). Note also that the remanence states obtained for this particle after applying a saturating fields along X and Z are identical (only the X state is plotted in Fig. 12b). In Particle 155 (the most extreme oblate particle), the remanence obtained after magnetizing along Y lies much closer to the major axis of the best fitting ellipsoid than the minor axis (Fig. 12c). A Type

II particle is shown in Fig. 12d. The angle between remanence pairs is small (16°) and the remanence lies at an intermediate angle between the minor and major axes of the best fitting ellipsoid, parallel to the average core orientation. A Type III particle is shown in Fig. 12e. The angle between remanence pairs is 56°, with the remanence lying close to the minor axis for fields applied along X and close to the major axis for fields applied along Z. In Type IV particles (not shown), the remanence generally lies closest to the major axis of the best-fitting ellipsoid. Those particles that show a change of domain type with field direction (Table 1) display a correspondingly wider range of possible remanence directions.

It is possible to access each of the four states by applying a suitably oriented saturating field. For example, applying saturating fields to Particle 155 along X and Y switches the sense of vortex rotation while retaining the direction of core magnetization (Fig. 12c). In small fields, the four states are separated by energy barriers that could, in principle, be overcome by thermal fluctuations. However, the energy barriers associated with switching the sense of vortex rotation while retaining the core direction (or switching the core direction while retaining the sense of vortex rotation) are likely to be very high compared to the barriers associated with switching both together. This is because the former process will require considerable internal disruption to the micromagnetic state and a correspondingly high exchange energy penalty, while the latter can be achieved simply by 180° rotation of the micromagnetic state against the shape anisotropy of the particle. Calculating these energy barriers is the next computational challenge, and will ultimately enable the acquisition of remanence during cooling of these particles to be modelled.

525

526 **3.3.3 Hysteresis loops.** Hysteresis loops are shown in Fig. 13 for selected particles and
527 applied field directions. The magnetic response of all particles is dominated by reversible
528 magnetization processes (e.g., the rotations of bulk spins towards the field). The
529 reversible component of magnetic susceptibility is highest (lowest) for fields applied
530 parallel to the major (minor) axis of the best-fitting ellipsoid. Irreversible magnetization
531 processes (e.g., nucleation of vortices, irreversible switching of vortex core position, core
532 orientation or core magnetization, changing sense of bulk spin rotation, denucleation of
533 vortices) produce small steps in magnetization superimposed on the large reversible
534 component. This leads to loops characterized by very low values of coercivity (H_c) and
535 squareness (M_{rs}/M_s). Highest coercivities (30-40 mT; Table 1) are observed in the small
536 Type 1 particles when fields are applied along X (e.g., antiparallel to the core direction,
537 close to the minor axis of the best-fitting ellipsoid; Fig. 13a). Typical coercivities are of
538 the order of a few mT or less (Fig. 13d). Negative values of coercivity listed in Table 1
539 highlight an unusual behavior (e.g., Fig. 13c), whereby the upper branch of the hysteresis
540 curve reaches the M = 0 axis at a positive applied field. This behavior leads to a self-
541 reversal of saturation isothermal remanent magnetization (SR-SIRM), in which a
542 component of saturation remanent magnetization is antiparallel to the saturating field
543 direction.

544 Despite the low M_{rs}/M_s values, the large volume of the particles means that their
545 total moments are at least equivalent to that of a 25 nm diameter SD particle, and in many
546 cases significantly greater (relative M_r values vary from ~1 up to ~44; Table 1). Despite
547 the low H_c values, the remanence states are also highly stable with respect to applied

548 fields. We define the stability of a remanence sate in terms of the 'minimum irreversible
549 field' (Table 1). To calculate this field, the spin state obtained at each negative field of
550 the upper hysteresis branch (from -10 to -1000 mT) was chosen as an initial
551 configuration, and the micromagnetic energy was minimized under zero field. The
552 minimum irreversible field is the smallest negative field required to produce a change in
553 the remanent state of the particle. Minimum irreversible fields are typically several
554 hundred mT, with several showing remanence states stable to more than 400 mT and one
555 simulation showing no significant change even up to 1000 mT. Note that the coercivity of
556 remanence (H_{cr}) is greater than or equal to the minimum irreversible field. Based on the
557 values in Table 1, all particles would plot in the MD region of a Day-Dunlop plot
558 (Dunlop 2002). However, such a comparison grossly misrepresents the remanence
559 carrying potential of these particles. Although the ratio of H_{cr}/H_c is similar to MD
560 samples, which make notoriously poor paleomagnetic recorders, the absolute values of
561 H_{cr} are at least an order of magnitude larger. Furthermore, MD materials have
562 vanishingly small values of the minimum irreversible field, since irreversible changes to
563 the remanent state of an MD material can be achieved by movement of weakly pinned
564 domain walls. For the vortex states studied here, no changes whatsoever are observed in
565 the remanence state until fields of several hundred mT are applied. A better comparison
566 of the remanence carrying potential of vortex states is obtained by first-order reversal
567 curve (FORC) analysis, which is not adversely affected by the large component of
568 reversible magnetization associated with the rotation of bulk spins. The range of
569 irreversible fields calculated here corresponds very well to the distribution of irreversible
570 magnetization observed in synthetic dusty olivine samples using FORC diagrams (Lappe

et al. 2011, 2013) and to the high stability of natural remanent magnetization with respect to alternating-field demagnetization observed by Fu et al. (2014). In comparison, FORC diagrams of MD materials typically show irreversible magnetization restricted to fields less than a few mT (Church et al. 2011; Lindquist et al. 2015) Unsurprisingly, the lowest irreversible fields observed here are for Type IV particles, which contain more MD-like structures. Even here, though, irreversible fields of 40-100 mT are typical.

4. Discussion

4.1. Rock magnetism of realistic ensembles

Conventional characterisation of the remanence carriers in rocks typically relies on either optical or SEM imaging of polished surfaces, or TEM imaging of thin foils. Although such 2D methods are an essential part of the qualitative characterisation process, our numerical simulations emphasise just how important 3D knowledge of particle geometry is for quantitative modelling. Shape and crystallographic orientation of an individual particle controls the orientation of its vortex core, or equivalently the position and type of its domain walls. Near the surface the bulk spins adapt to the faceting of the particle. In symmetric particles, we might expect that the bulk spins cancel each other out and that the total remanence would be dominated by uncompensated spins within the core. A striking example of where this assumption breaks down is shown in Fig. 14 (Particle 155, a Type I particle with a pronounced oblate geometry). In this case, the core is parallel to the minor axis of the best-fitting ellipsoid, but the net remanence lies at a large angle to this, and rotates by 80° as the sense of bulk spin rotation changes

(Fig. 12c). The explanation for this behaviour is the combination of the short length of the core, which reduces its contribution to the net moment, and the uneven length of opposing surface facets, which creates a significant contribution from uncompensated bulk spins. In Fig. 14, this unbalancing is highlighted by plotting the anisotropy energy of the domain walls. The width of the walls and the sizes of the four resulting quadrants can be seen to be of unequal sizes. In the configuration shown, there are more spins pointing along +Z due to the larger facet on right than there are compensating spins along –Z due to the small facet on the left. A similar situation is known for vortex states in sufficiently large uniaxial particles, where several metastable magnetization states may exist that are related to edge moments that can be aligned parallel or anti-parallel to the global demagnetizing field (Fig. 7 in Rave et al. 1998). The importance of bulk spins in controlling the remanence of vortex states in particles with realistic morphologies is not generally appreciated.

The sheet-like arrangement of particles within the reconstructed volume (Fig. 4) is expected to generate significant remanence anisotropy. Such anisotropy is well documented in single-crystal paleomagnetism studies (Feinberg et al. 2004, 2005; Fu et al. 2014) and must be corrected before the measured remanence directions can be interpreted quantitatively. Fu et al. (2014) measured the anisotropy of ARM susceptibility for the same grain studied here (Fig. 7), finding normalised values of 0.45, 0.56 and 1 for the minimum, intermediate and maximum susceptibilities, respectively. The maximum ARM susceptibility is observed for fields applied along Z, which corresponds to the average orientation of major ellipsoid axes. This observation is most consistent with remanence carried by prolate Type III and IV particles and oblate Type I particles such as

616 those shown in Fig. 14, and suggests that such particles are more prevalent in regions of
617 the grain outside the reconstructed volume. The fact that the minimum susceptibility axis
618 is not aligned with the average orientation of minor axes is explained by the presence of
619 Type I and II particles, which contribute to the remanence when fields are applied normal
620 to the sheets. A full model of the entire ensemble, taking into account the magnetostatic
621 interaction fields between particles and the distribution of shape anisotropy, would be
622 necessary to fully describe the anisotropic response of the system (Hargraves et al. 1991)
623 as well as accounting for the presence of much larger particles that may occur outside the
624 analysed volume. Such calculations could serve to improve dramatically the
625 interpretation of single-crystal paleomagnetic studies, and minimise the number of repeat
626 measurements needed to reach a statistical significance equivalent to bulk paleomagnetic
627 studies.
628

629 **4.2 Implications for chondrite paleomagnetism**

630 This study demonstrates that particles in the lower half of the size distribution
631 adopt a single vortex state (Type I and II), with the larger particles adopting Type III and
632 IV (i.e., emerging MD) behaviour. Lappe et al. (2011) similarly identified a dominance of
633 single vortex states, but noted also a significant number of SD particles. It appears that
634 the size distribution of particles in synthetic dusty olivine is shifted to smaller values than
635 the natural sample studied here. Nevertheless, given the abundance of single vortex states
636 in both cases, calibrations of non-heating paleointensity methods using synthetic dusty
637 olivine (Lappe et al. 2013) remain largely valid. Similarly, given the high field stabilities
638 observed here for single vortex states (Table 1), the conclusion that dusty olivine is

capable of recording and maintaining a faithful record of pre-accretionary remanence (Lappe et al. 2011) also remains valid. Indeed, the combination of high switching fields and large volumes of single vortex states should translate to carriers with very high thermal stability (i.e. high blocking temperatures). High thermal stability of vortex states at temperatures up to the Curie temperature has recently been demonstrated in magnetite using electron holography(Almeida et al. 2014, 2016). In principle, micromagnetic simulations can be used to calculate energy barriers between alternate remanence states, and thereby model the acquisition of thermoremanent magnetization. Such calculations are beyond the scope of the present study, but are an obvious next step in the nanopaleomagnetic approach.

5. Outlook and Implications

FIB-nT reveals not only the true size and shape distribution of individual particles, but also the required mesoscale information at the ensemble level. The spatial resolution is good enough to detect particles that span the SD to PSD range (the size range of most importance in rock magnetism) and the volume of sample accessible by FIB-nT approaches the volumes that can now be detected paleomagnetically using SQUID microscopy (i.e. tens of microns). A long-term goal of rock magnetism is to understand the collective behaviour of particle ensembles based on fundamental physical principles. Some recent progress in this area has been made (Harrison and Lascu 2014), but current models are still reliant on the assumption of uniaxial, single-domain behaviour. The combination of FIB-nT and finite-element micromagnetics goes some way towards bridging the gap between what we currently model and how samples

actually behave in the real world. We are still some way, however, from a general ensemble model that captures the intricacies of the PSD state.

Acknowledgements

The research leading to these results has received funding from the European Research Council under the European Union's Seventh Framework Programme (FP/2007-2013)/ ERC grant agreements 291522 - 3DIMAGE (P.A.M.) and 320750 – Nanopaleomagnetism (J.F.E., R.J.H., and P.A.M.). BPW and RRF were supported by NASA Emerging Worlds program grant #NNX15AH72G, the NASA Solar System Exploration and Research Virtual Institute grant #NNA14AB01A, and a generous gift from Thomas F. Peterson, Jr. The research leading to these results has received funding from the European Research Council under the European Union's Seventh Framework Programme (FP/2007-2013) / ERC Grant Agreement No. 320832- Imagine. (W.W. and P.O.C.)

References

Almeida, T.P., Kasama, T., Muxworthy, A.R., Williams, W., Nagy, L., and Dunin-Borkowski, R.E. (2014) Observing thermomagnetic stability of nonideal magnetite particles: Good paleomagnetic recorders? Geophysical Research Letters, 41, 7041–7047.

Almeida, T.P., Muxworthy, A.R., Kovacs, A., Williams, W., Brown, P.D., and Dunin-Borkowski, R.E. (2016) Direct visualization of the thermomagnetic behavior of

684 pseudo-single-domain magnetite particles. Science Advances, 2, e1501801–
685 e1501801.
686 Bera, B., Mitra, S.K., and Vick, D. (2011) Understanding the micro structure of Berea
687 Sandstone by the simultaneous use of micro-computed tomography (micro-CT) and
688 focused ion beam-scanning electron microscopy (FIB-SEM). Micron (Oxford,
689 England□: 1993), 42, 412–8.
690 Bushby, A.J., P'ng, K.M.Y., Young, R.D., Pinali, C., Knupp, C., and Quantock, A.J.
691 (2011) Imaging three-dimensional tissue architectures by focused ion beam scanning
692 electron microscopy. Nature protocols, 6, 845–58.
693 Carriero, A., Doube, M., Vogt, M., Busse, B., Zustin, J., Levchuk, A., Schneider, P.,
694 Müller, R., and Shefelbine, S.J. (2014) Altered lacunar and vascular porosity in
695 osteogenesis imperfecta mouse bone as revealed by synchrotron tomography
696 contributes to bone fragility. Bone, 61, 116–24.
697 Church, N., Feinberg, J.M., and Harrison, R. (2011) Low-temperature domain wall
698 pinning in titanomagnetite: Quantitative modeling of multidomain first-order
699 reversal curve diagrams and AC susceptibility. Geochemistry, Geophysics,
700 Geosystems, 12.
701 Connolly, H., Jones, B., and Hewins, R. (1998) The flash melting of chondrules: an
702 experimental investigation into the melting history and physical nature of chondrule
703 precursors. Geochimica Et Cosmochimica Acta, 62, 2725–2735.
704 Crewe, A. V., and Nellist, P.D. (2009) The Scanning Transmission Electron Microscope.
705 In J. Orloff, Ed., Handbook of Charged PArticle Optics pp. 497–522.
706 De Winter, D.A.M., Schneijdenberg, C.T.W.M., Lebbink, M.N., Lich, B., Verkleij, A.J.,

Drury, M.R., and Humbel, B.M. (2009) Tomography of insulating biological and geological materials using focused ion beam (FIB) sectioning and low-kV BSE imaging. Journal of microscopy, 233, 372–83.

Doube, M., Kłosowski, M.M., Arganda-Carreras, I., Cordelières, F.P., Dougherty, R.P., Jackson, J.S., Schmid, B., Hutchinson, J.R., and Shefelbine, S.J. (2010) BoneJ: Free and extensible bone image analysis in ImageJ. Bone, 47, 1076–9.

Fabian, K., Kirchner, A., Williams, W., Heider, F., Leibl, T., and Huber, A. (1996) Three-dimensional micromagnetic calculations for magnetite using FFT. Geophysical Journal International, 124, 89–104.

Feinberg, J.M., Wenk, H.R., Renne, P.R., and Scott, G.R. (2004) Epitaxial relationships of clinopyroxene-hosted magnetite determined using electron backscatter diffraction (EBSD) technique. American Mineralogist, 89, 462–466.

Feinberg, J.M., Scott, G.R., Renne, P.R., and Wenk, H.-R. (2005) Exsolved magnetite inclusions in silicates: Features determining their remanence behavior. Geology, 33, 513.

Flinn, D. (1962) On folding during three-dimensional progressive deformation. Quarterly Journal of the Geological Society, 118, 385–428.

Fu, R.R., Weiss, B.P., Lima, E.A., Harrison, R.J., Bai, X.-N., Desch, S.J., Ebel, D.S., Suavet, C., Wang, H., Glenn, D., and others (2014) Solar nebula magnetic fields recorded in the Semarkona meteorite. Science, 346, 1089–1092.

Gilbert, P. (1972) Iterative methods for the three-dimensional reconstruction of an object from projections. Journal of Theoretical Biology, 36, 105–117.

Hargraves, R.B., Johnson, D., and Chan, C.Y. (1991) Distribution anisotropy: The cause

of AMS in igneous rocks? Geophysical Research Letters, 18, 2193.

Harrison, R.J., and Lascu, I. (2014) FORCulator: A micromagnetic tool for simulating first-order reversal curve diagrams. Geochemistry, Geophysics, Geosystems, 15, 4671–4691.

Hewins, R., Connolly, H., Lofgren, G., and Libourel, G. (2005) Experimental constraints on chondrule formation, 341, 286–316.

Holzer, L., and Cantoni, M. (2012) REVIEW OF FIBTOMOGRAPHY. In I. Utke, S. Moshkalev, and P. Russell, Eds., Nanofabrication Using Focused Ion and Electron Beams Principles and Applications pp. 410–435.

Holzer, L., Indutnyi, F., Gasser, P.H., Münch, B., and Wegmann, M. (2004) Three-dimensional analysis of porous BaTiO3 ceramics using FIB nanotomography. Journal of microscopy, 216, 84–95.

Hubert, A. (1967) Der Einfluß der Magnetostriktion auf die magnetische Bereichsstruktur einachsiger Kristalle, insbesondere des Kobalts. physica status solidi (b), 22, 709–727.

Hubert, A., and Rave, W. (1999) How well-defined are closure domains? Journal of Magnetism and Magnetic Materials, 197, 325–326.

Hubert, A., and Schäfer, R. (1998) Magnetic Domains: The Analysis of Magnetic Microstructures, 1st ed. Springer Science & Business Media.

Keller, L.M., Holzer, L., Wepf, R., and Gasser, P. (2011a) 3D geometry and topology of pore pathways in Opalinus clay: Implications for mass transport. Applied Clay Science, 52, 85–95.

Keller, L.M., Holzer, L., Wepf, R., Gasser, P., Münch, B., and Marschall, P. (2011b) On

753 the application of focused ion beam nanotomography in characterizing the 3D pore
754 space geometry of Opalinus clay. Physics and Chemistry of the Earth, Parts A/B/C,
755 36, 1539–1544.
756 Kirby, S.H., and Wegner, M.W. (1978) Dislocation substructure of mantle-derived
757 olivine as revealed by selective chemical etching and transmission electron
758 microscopy. Physics and Chemistry of Minerals, 3, 309–330.
759 Kruhl, J.H., Wirth, R., and Morales, L.F.G. (2013) Quartz grain boundaries as fluid
760 pathways in metamorphic rocks. Journal of Geophysical Research: Solid Earth, 118,
761 1957–1967.
762 Landrot, G., Ajo-Franklin, J.B., Yang, L., Cabrini, S., and Steefel, C.I. (2012)
763 Measurement of accessible reactive surface area in a sandstone, with application to
764 CO2 mineralization. Chemical Geology, 318-319, 113–125.
765 Lappe, S.-C.L.L., Church, N.S., Kasama, T., da Silva Fanta, A.B., Bromiley, G., Dunin-
766 Borkowski, R.E., Feinberg, J.M., Russell, S., and Harrison, R.J. (2011) Mineral
767 magnetism of dusty olivine: A credible recorder of pre-accretionary remanence.
768 Geochemistry, Geophysics, Geosystems, 12, n/a–n/a.
769 Lappe, S.-C.L.L., Feinberg, J.M., Muxworthy, A., and Harrison, R.J. (2013) Comparison
770 and calibration of nonheating paleointensity methods: A case study using dusty
771 olivine. Geochemistry, Geophysics, Geosystems, 14, 2143–2158.
772 Lee, E.W. (1955) Magnetostriction and Magnetomechanical Effects. Reports on Progress
773 in Physics, 18, 184–229.
774 Leroux, H., Libourel, G., Lemelle, L., and Guyot, F. (2003) Experimental study and TEM
775 characterization of dusty olivines in chondrites: Evidence for formation by in situ

776 reduction. Meteoritics & Planetary Science, 38, 81–94.
777 Lindquist, A.K., Feinberg, J.M., Harrison, R.J., Loudon, J.C., and Newell, A.J. (2015)
778 Domain wall pinning and dislocations: Investigating magnetite deformed under
779 conditions analogous to nature using transmission electron microscopy. Journal of
780 Geophysical Research: Solid Earth, 120, 1415–1430.
781 Muxworthy, a. R., and Williams, W. (2015) Critical single-domain grain sizes in
782 elongated iron particles: implications for meteoritic and lunar magnetism.
783 Geophysical Journal International, 202, 578–583.
784 Radeloff, C. (1964) The Determination Of The Six Magnetostriction Constants Of Iron. Z
785 Angew Phys, 17, 247–253.
786 Rave, W., Fabian, K., and Hubert, A. (1998) Magnetic states of small cubic particles with
787 uniaxial anisotropy. Journal of Magnetism and Magnetic Materials, 190, 332–348.
788 Schiffbauer, J.D., and Xiao, S. (2009) Novel application of focused ion beam electron
789 microscopy (FIB-EM) in preparation and analysis of microfossil ultrastructures: A
790 new view of complexity in early Eukaryotic organisms. PALAIOS, 24, 616–626.
791 Schindelin, J., Arganda-Carreras, I., Frise, E., Kaynig, V., Longair, M., Pietzsch, T.,
792 Preibisch, S., Rueden, C., Saalfeld, S., Schmid, B., and others (2012) Fiji: an open-
793 source platform for biological-image analysis. Nature methods, 9, 676–82.
794 Uehara, M., and Nakamura, N. (2006) Experimental constraints on magnetic stability of
795 chondrules and the paleomagnetic significance of dusty olivines. Earth and
796 Planetary Science Letters.
797 Weiss, B.P., Lima, E.A., Fong, L.E., and Baudenbacher, F.J. (2007) Paleomagnetic
798 analysis using SQUID microscopy. Journal of Geophysical Research, 112, B09105.

Weiss, B.P., Gattacceca, J., Stanley, S., Rochette, P., and Christensen, U.R. (2010) Paleomagnetic Records of Meteorites and Early Planetesimal Differentiation. Space Science Reviews, 152, 341–390.

Williams, D.B., and Carter, C.B. (2002) Transmission Electron Microscopy. Characterization of Materials. Springer Science.

Williams, W., and Fabian, K. (2016) MERRILL: A finite element micromagnetic modeling package for rock magnetism. In Prep.

Figure Captions

Figure 1 (a) SEM micrograph of Semarkona Dusty Olivine Grain DOC5. White box indicates region used for FIB-nT and S/TEM studies. (b) Top down FIB micrograph of FIB-nT MROI after trenches have been milled. Hourglass structure is a fiducial mark to assist in mill pattern placement. (c-e) The cyclic sequence of steps for each 20 nm slice in FIB-nT volume collected.

Figure 2 (a) BSE SEM micrograph from slice 151 where medium grey is olivine and the light grey are the Fe nanoparticles. Also visible are non-crystalline materials such as charging of amorphous silica (saturated white) and holes and/or uncharged silica (saturated black). (b) Binary segmented image of same BSE image after denoising and manual artefact removal this leaves particles as white voxels and all other materials as black.

822 **Figure 3** Transformation of tomographic particle voxels into tetrahedral meshes for FEM
823 modelling for particle number 8, the smallest prolate particle captured in the FIB-nT
824 volume. (a) Initially the individual particles form a rough box like volume, described by
825 the voxels of the original FIB-nT volume. (b) By fitting a bounding polyhedron subject to
826 the Poisson equation, a rough triangular surface mesh is generated. (c) Applying a
827 smoothing filter to the Poisson surface results in a mesh with triangular nodes spaced
828 every < 2.5 nm. This is too high a mesh density for efficient micromagnetic modelling.
829 (c) Using a Delaunay triangulation function, the surface mesh is coarsened to the desired
830 5 nm-resolution triangular surface mesh. This surface is then used to seed the interior
831 tetrahedral elements of the same size.
832
833 **Figure 4** Orthogonal views of the reconstructed volume on the (a) X-Y plane, (b) X-Z
834 plane and (c) Y-Z plane. (d**)** Close up detail of several larger particles where faceting is
835 observable.
836
837 **Figure 5** Histograms of best-fitting ellipsoid diameters for the (a) major, (b) intermediate
838 and (c) minor axes of each Fe particle in the FIB-nT reconstruction.
839
840 **Figure 6 (a)** Flinn plot of the particle aspect ratios. The 45° line describes particles with a
841 Flinn ratio of 1. The particle aspect ratios are plotted with colour and point size scaling as
842 a function of the major radius length in nanometres. (b) Histogram of Flinn ratios (<1 for
843 oblate, > 1 for prolate) from the FIB-nT volume.
844

Figure 7 Stereographic projection showing the orientation of major (red circles), intermediate (green circles) and minor (blue circles) axes of the best-fitting ellipsoids. Open circles are upper hemisphere, closed circles are lower hemisphere. The three solid triangles plot the measured the anisotropy of ARM susceptibility for the entire dusty olivine grain studied (Maximum susceptibility is red, intermediate is green and minor is blue).

Figure 8 STEM bright field montage showing Fe particles (dark), olivine (grey) and silica blebs (bright). Sub-grains are visible as small changes in grey scale in the olivine host. Blue inset shows a bright-field TEM image of the highlighted Fe nanoparticle. Faceting parallel to sub-grain boundaries, defined by multiple dislocations, can be observed. Red inset: upper left panel shows bright-field TEM of the two highlighted Fe nanoparticles; upper right panel shows the diffraction pattern of olivine matrix collected at an α ftilt of -3.5° and a β -tilt of -1.1°; lower left panel shows the diffraction pattern for the smaller Fe particle; lower right panel shows the STEM tomographic reconstruction of the smaller Fe nanoparticle.

Figure 9 The four types of pseudo-single domain state observed in the FEM simulations. Colorbar for arrows shows the direction and magnitude of the normalized M_z component of the particle magnetization. Green isosurfaces are selected to highlight the magnitude of the vorticity of the moment vector field. These vary particle to particle and are selected to present the minimum continuous surface. (a) Type I: single vortex with core oriented parallel to the minor axis of the best-fitting ellipsoid for particle 155. (b) Type II: single

868 vortex with core oriented within the plane defined by the minor and major axes of the
869 best-fitting ellipsoid for particle 165. (c) Type III: single vortex with core oriented
870 parallel to the major axis of the best-fitting ellipsoid for particle 75. (d) Type IV: multiple
871 core/wall-like structures for particle 233 with the magnetic field applied along the Y and
872 Z-axis respectively.
873
874 **Figure 10** Evolution of vortex core morphology. (a) The vortex core of particle 48
875 plotted for a helicity level of 180. (b) The vortex core of particle 165 plotted for a helicity
876 level of 40. (c) The vortex core of particle 8 plotted for a helicity level of 80. (d) The
877 vortex core of particle 75 plotted for a helicity level of 75.
878
879 **Figure 11** Thresholded anisotropy energy surfaces for particle 233, showing wall regions
880 corresponding to the highest magnetocrystalline anisotropy energy. The color of each
881 surface represents the projection of wall magnetization along the minor axis of the best-
882 fitting ellipsoid (~ parallel to X). Red is positive, blue is negative. (a) Type III remanence
883 state resulting from magnetic field applied along the X-axis. Dashed green line shows
884 approximate position of cross-section in (c). (b) Type IVa remanence state resulting from
885 magnetic field applied along the Y-axis. (c) Cross section through the anisotropy surface
886 in (a). (d) Type IVb remanence state displaying well-defined 90° walls resulting from
887 magnetic field applied along the Z-axis.
888
889 **Figure 12** (a) Schematic drawing depicting the four possible combinations of bulk spin
890 rotation and vortex core direction. (b-e) Stereograms showing the remanence vectors

obtained after applying fields along X (black circle), Y (black square) and Z (black triangle). Diamonds show the orientation of major (red), intermediate (green) and minor (blue) axes of the best-fitting ellipsoid. Lines show the traces of planes normal to the corresponding axes of the best-fitting ellipsoid. Closed symbols and solid lines are lower hemisphere; open symbols and dashed lines are upper hemisphere. Results are shown for two Type I particles (b, c); (d) a Type II particle; and (e) a type III particle. Note also that the remanence states obtained for this particle after applying a saturating fields along X and Z are identical (only the X state is plotted in Fig. 12b).

Figure 13 Calculated components of magnetization parallel to X (blue), Y (green) and Z (red) as a function of applied field for the upper (solid) and lower (dashed) branches of the major hysteresis loop. (a) Type I particle (364) with field applied along X. (b) Type I particle (48) with field applied along Y. (c) Type I particle (48) with field applied along Z. (d) Type III particle (233) with field applied along X.

Figure 14 Thresholded anisotropy energy surface for particle 155, showing wall regions corresponding to the highest magnetocrystalline anisotropy energy. The color of each surface represents the projection of wall magnetization along the minor axis of the best-fitting ellipsoid (~ parallel to X). Red is positive, blue is negative. Note the larger size of the right hand domain (red) compared to the left hand domain (blue) is due to the different size of the corresponding surface facets, and leads to a net contribution to the remanence of the particle from the bulk spins.

914

915 **Tables**

Particle ID	Major radius (nm)	Inter. radius (nm)	Minor radius (nm)	Flinn Ratio	Mesh Vol. (nm^3)	M_{rs}/M_s X Y Z	H_c (mT) X Y Z	Rel. M_r	Min. Irrev. Field (mT)	Domain state
STEM	119	117	98	0.85	5.72E +06	0.0086 0.0086 0.0086	0.2 0.5 7	6 6 6	270 330 260	II II II
48	36	35	23	0.68	1.43E +05	0.066 0.065 -0.067	42 19 -20	1.16 1.14 1.16	260 310 300	I I I
321	54	44	28	0.78	2.97E +05	0.032 0.036 -0.032	27 2.1 -4.4	1.15 1.32 1.15	380 260 410	I I I
364	34	26	16	0.8	2.46E +05	0.042 -0.03 -0.042	37 -5 -4	1.27 0.9 1.27	290 300 >1000	I I I
8	138	79	54	1.2	2.24E +06	0.012 0.022 0.022	11 8 5	3.1 6.1 6.1	440 260 240	III III III
233	536	163	71	1.43	2.27E +07	0.013 0.016 0.0035	8 4 0.5	36.7 44.8 9.7	230 60 100	III IVa IVb
75	259	133	84	1.23	1.13E +07	0.0059 0.016 0.018	6 4 6	8.1 21.7 25.8	430 260 40	III III IVa
165	262	228	151	0.76	3.73E +07	0.0027 0.0035 0.0035	2.5 0.64 0.04	12.2 16 16	250 330 490	II II II
155	213	198	73	0.4	1.33E +07	0.004 -0.003 0.004	3.6 -0.09 1.1	7 5.6 7	500 260 300	I I I

916
917

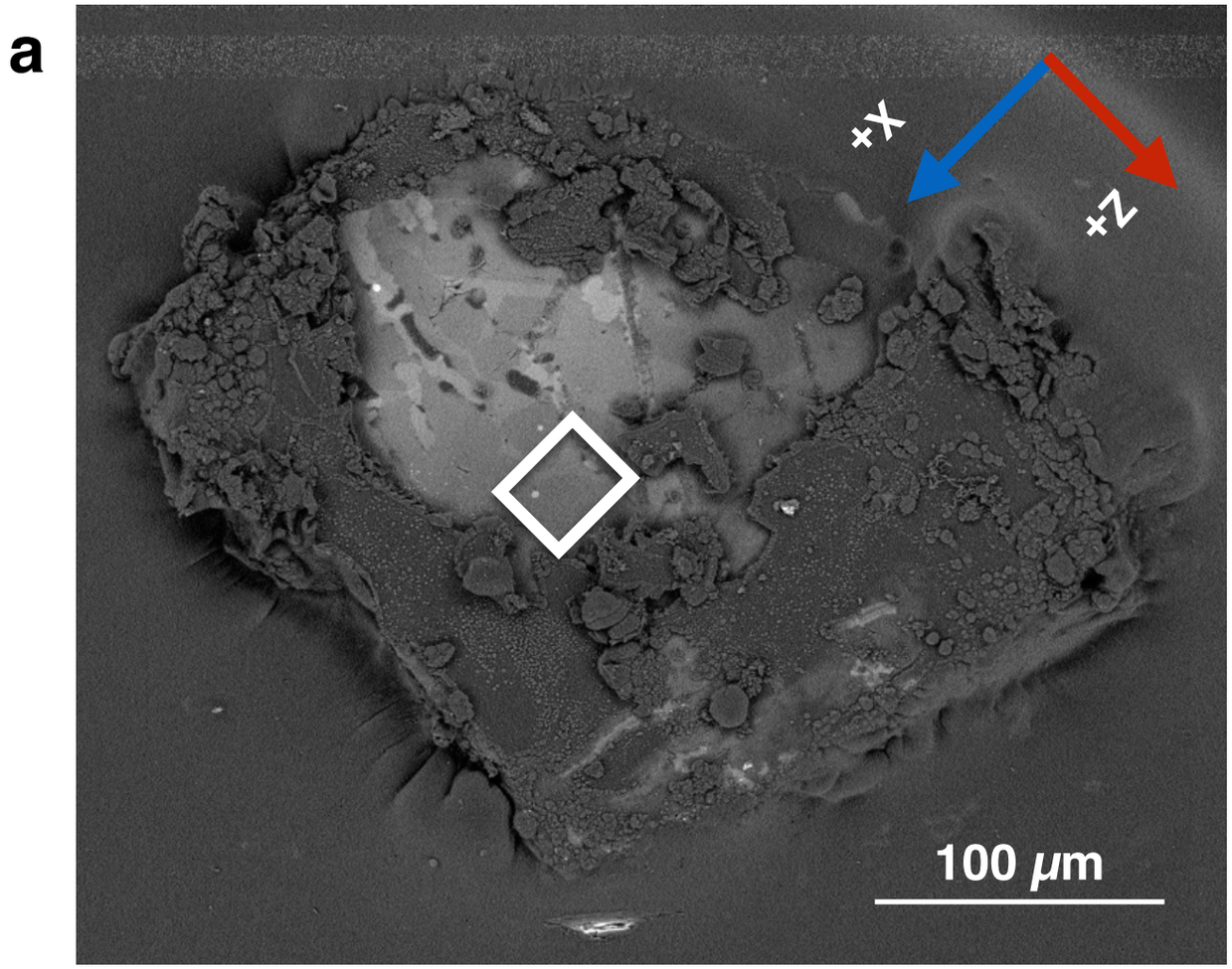

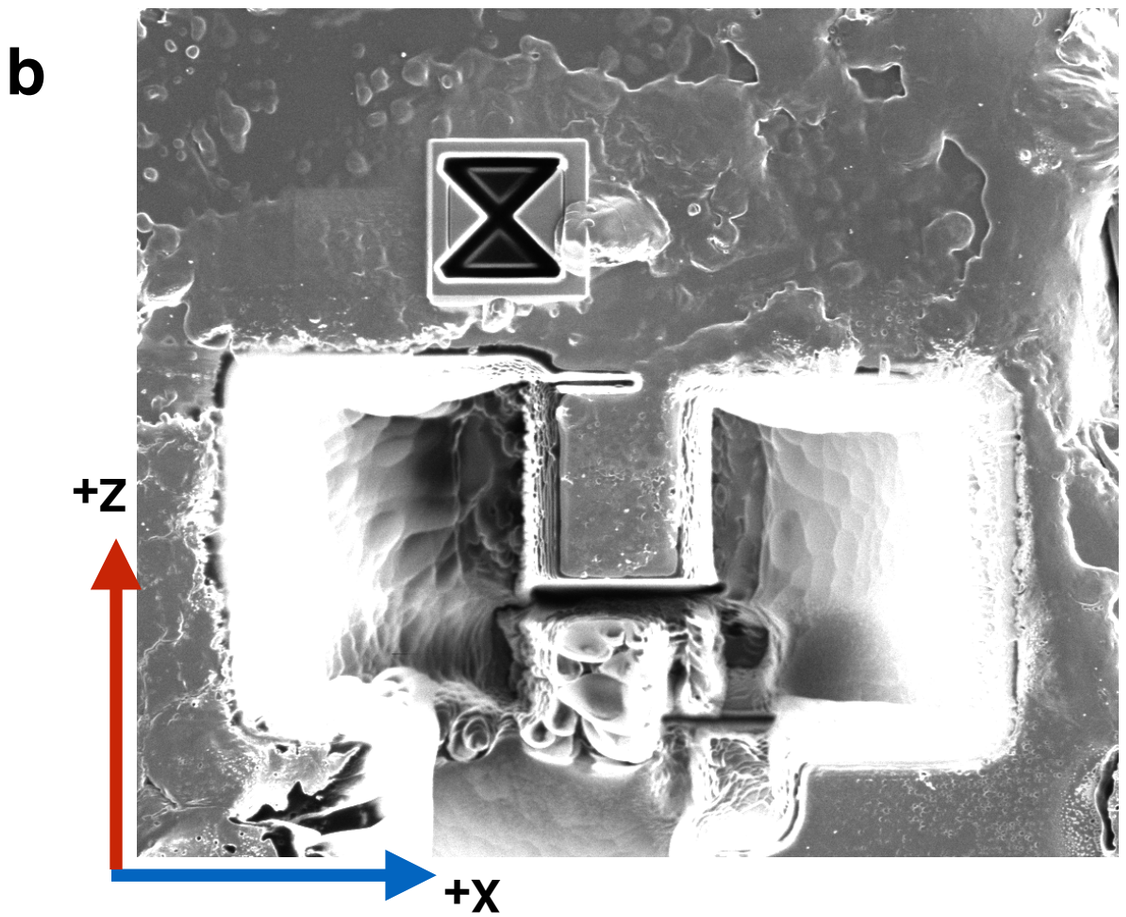

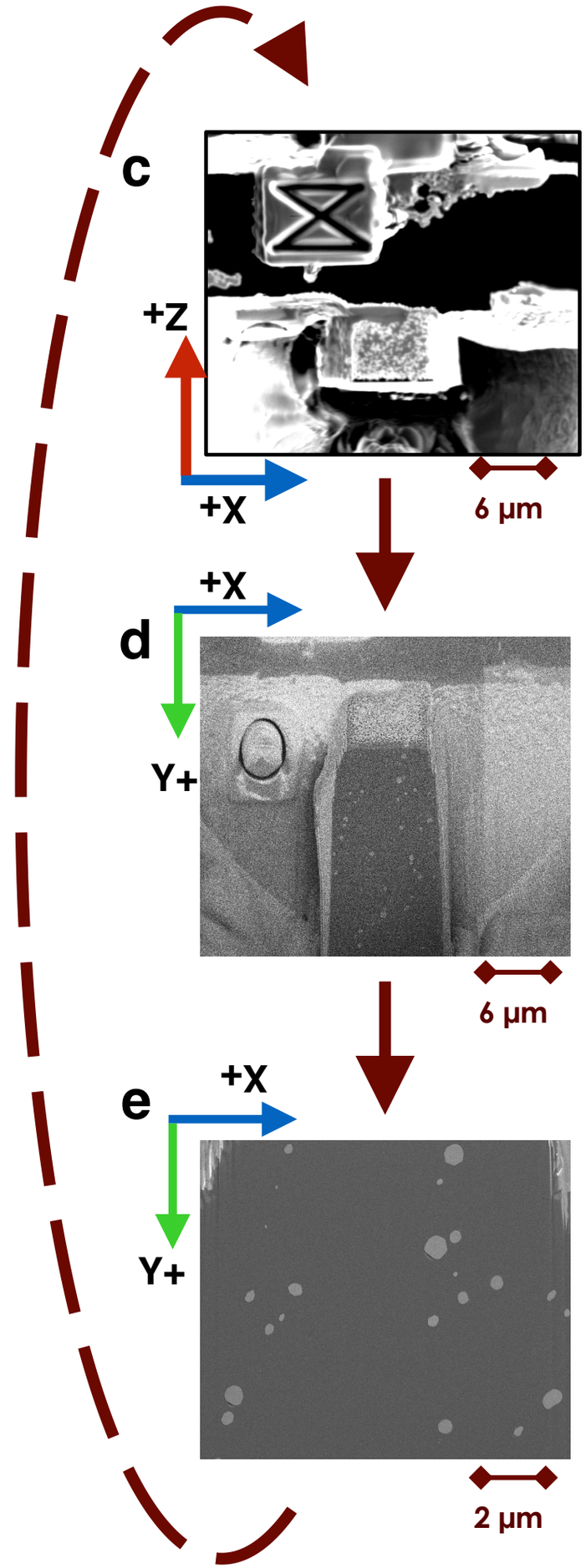

Figure 1

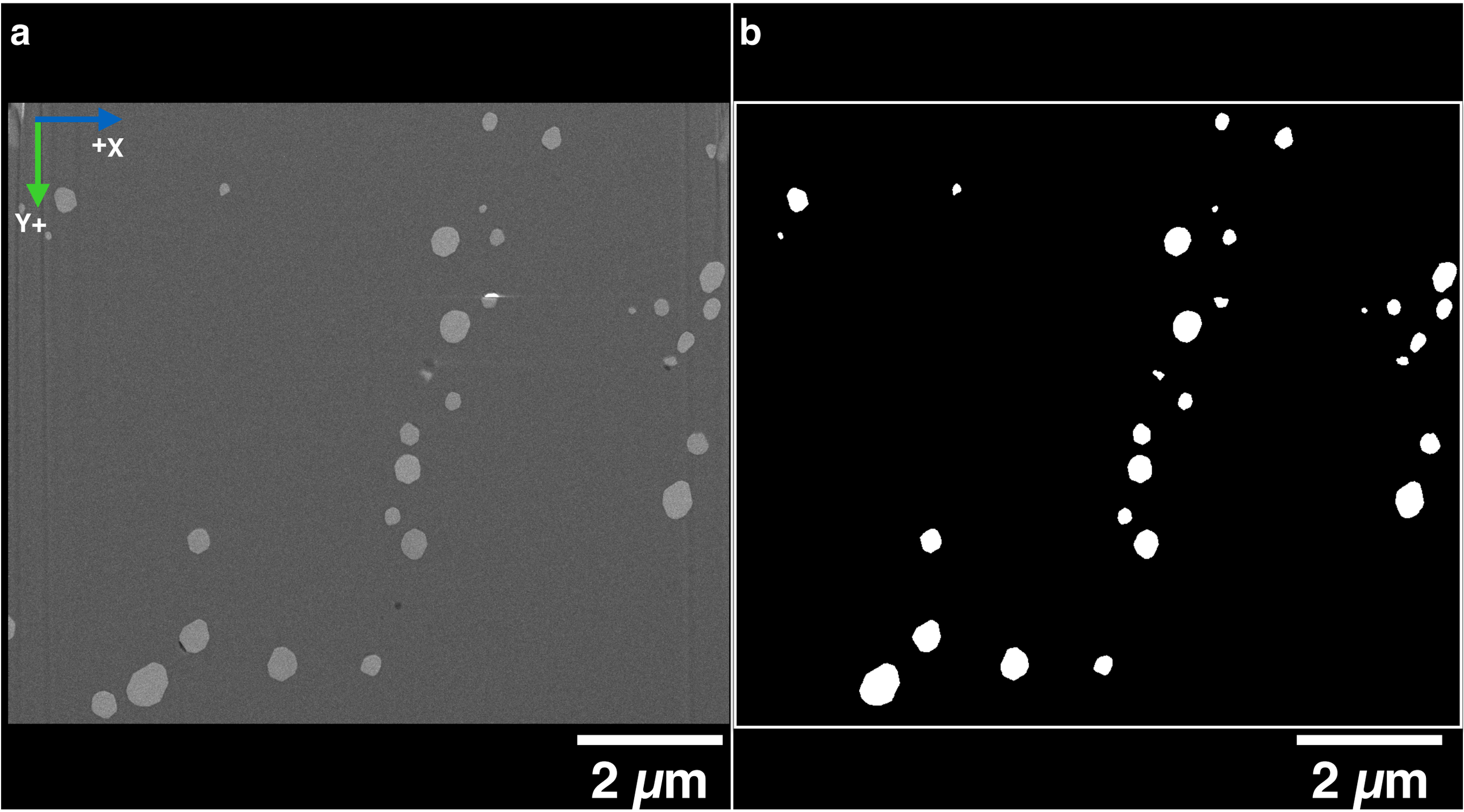

Figure 2

Figure 3

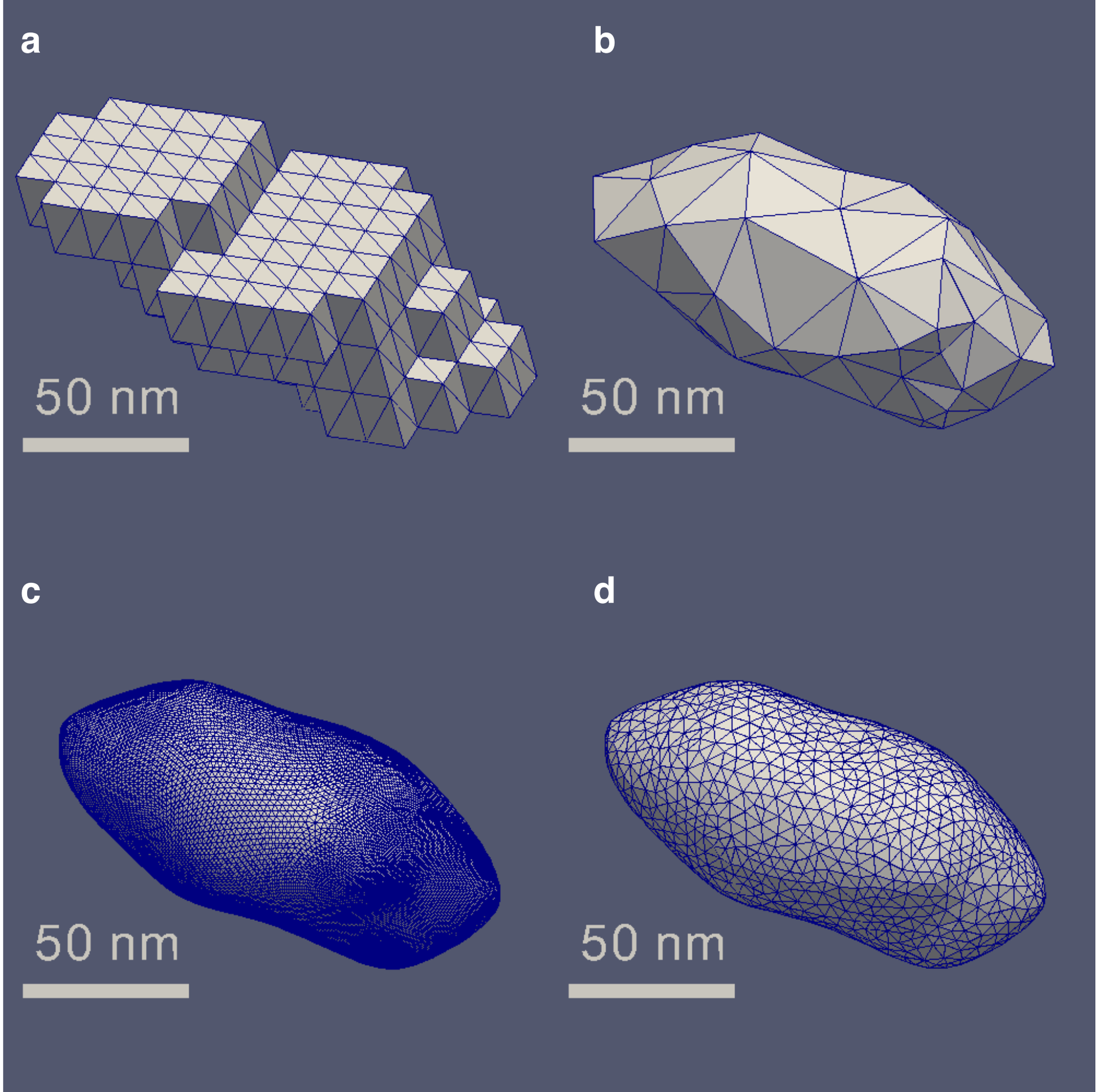

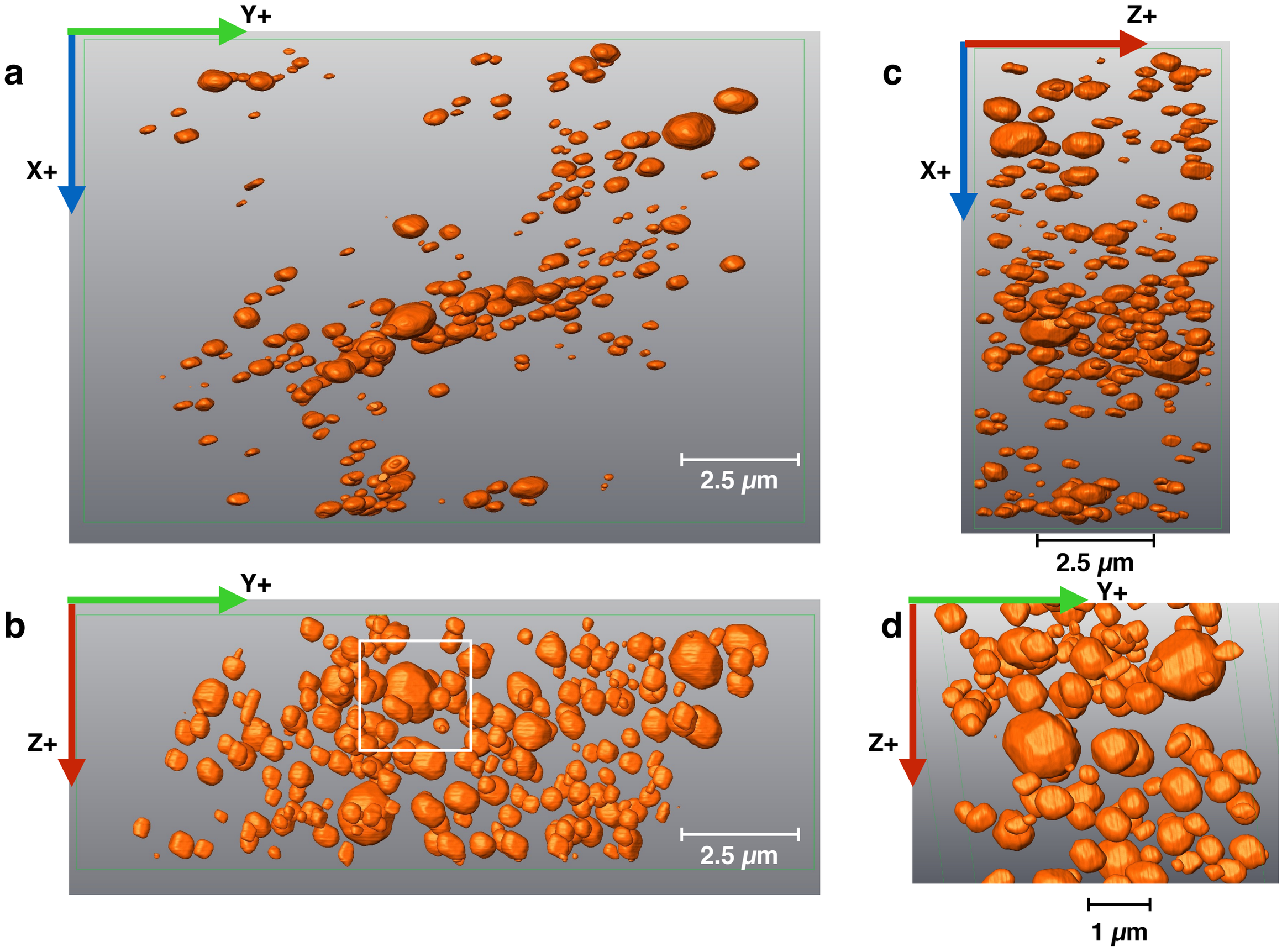

Figure 4

Figure 5

a

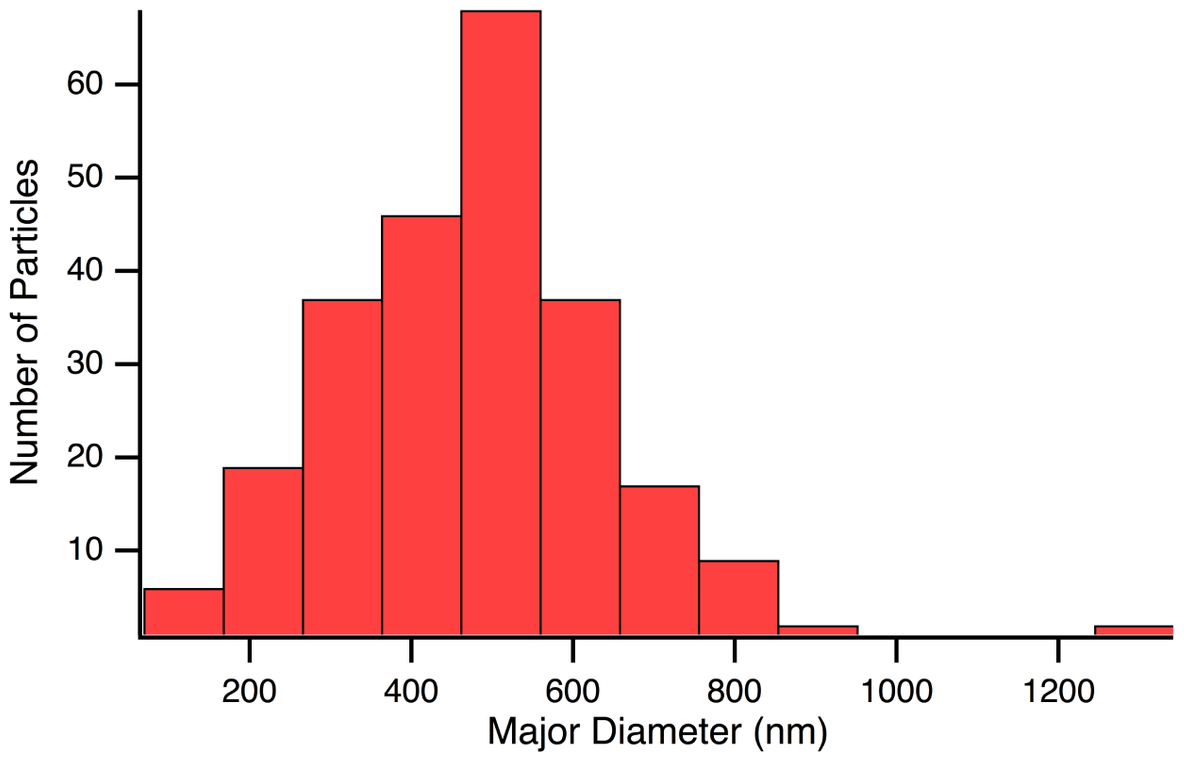
Number of Particles
60
50
40
30
20
10
200
400
600
800
1000
1200
Major Diameter (nm)

b

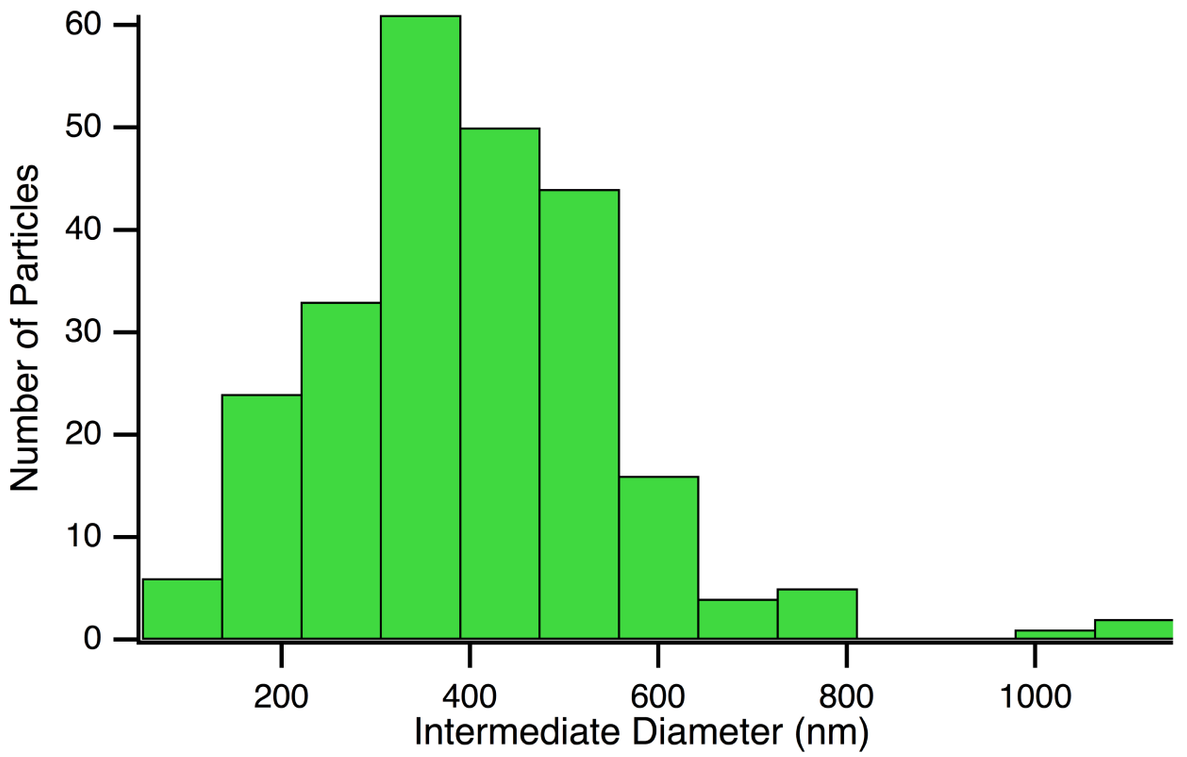
Number of Particles
60
50
40
30
20
10
0
200
400
600
800
1000
Intermediate Diameter (nm)

c

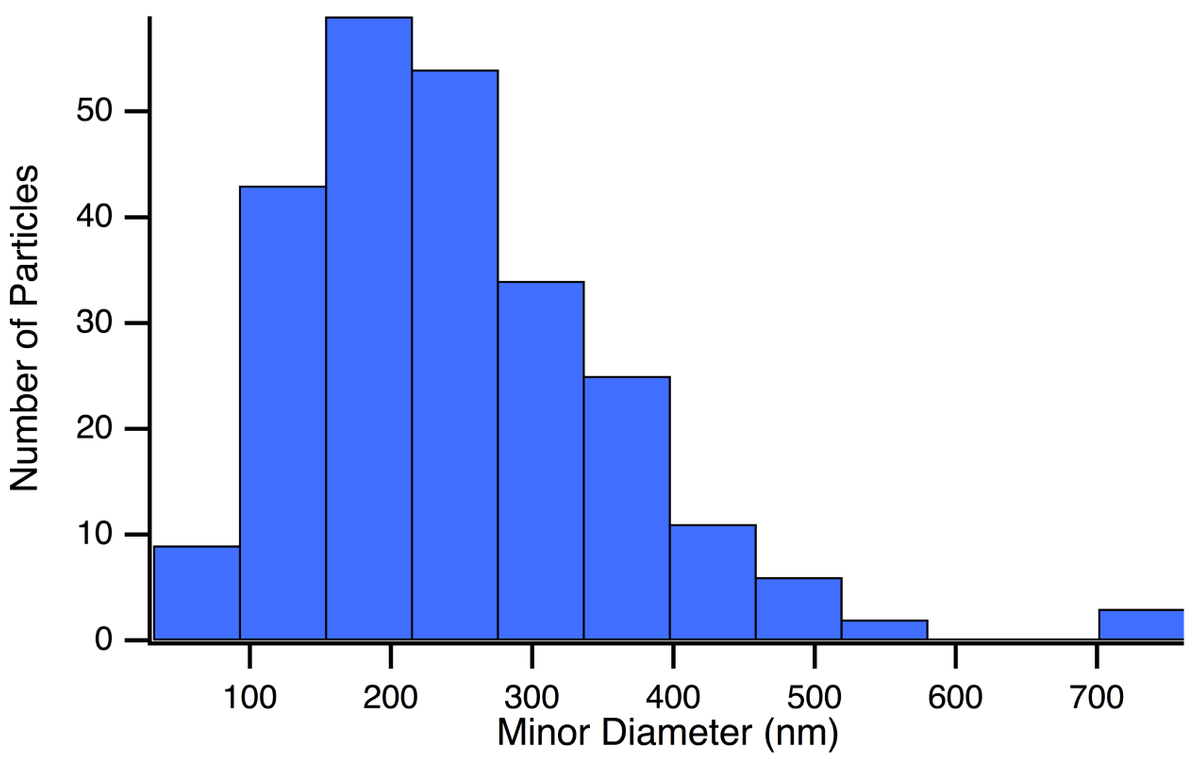
Number of Particles
50
40
30
20
10
0
100
200
300
400
500
600
700
Minor Diameter (nm)

Figure 6

a

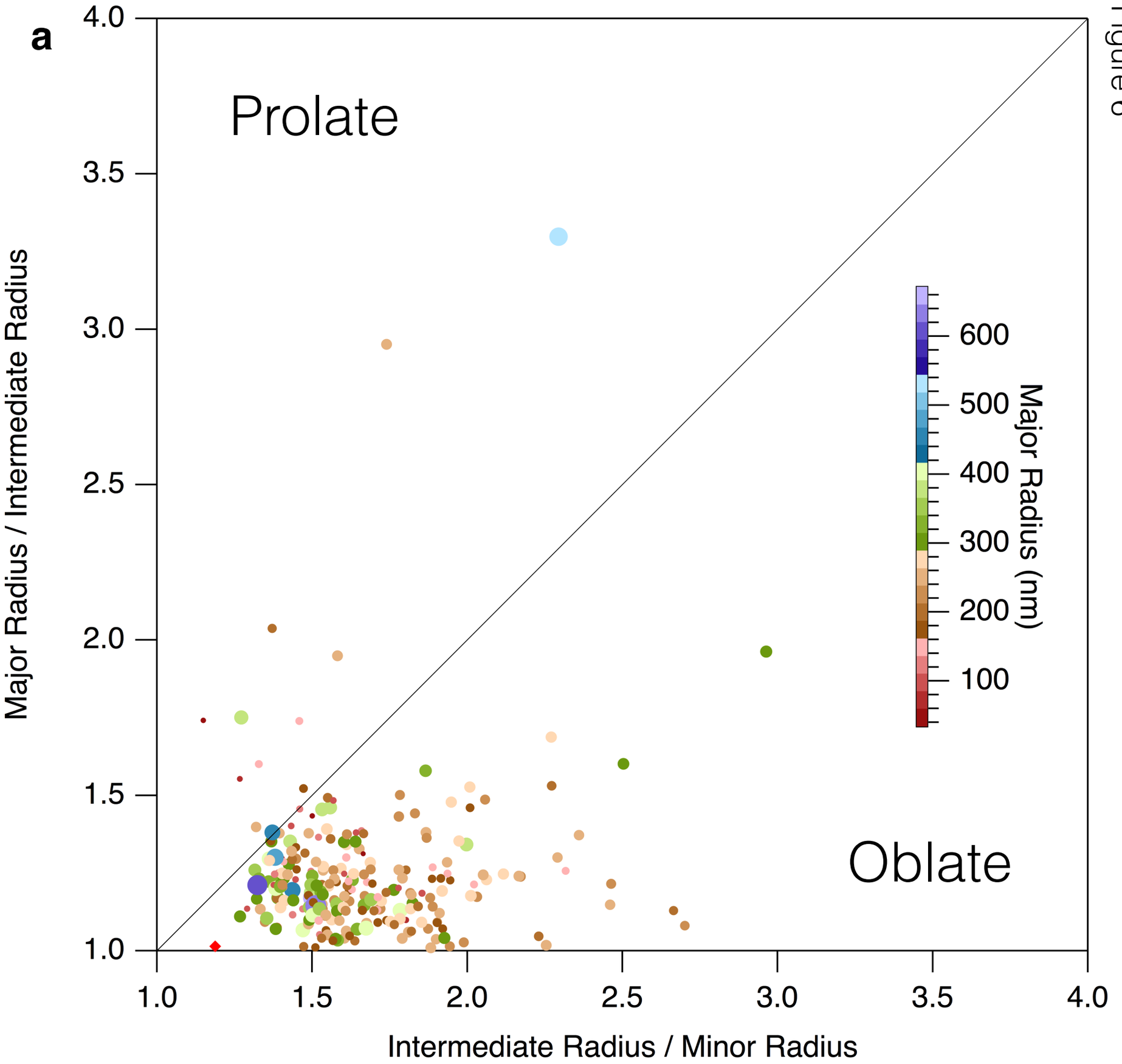
Prolate
Oblate
Major Radius / Intermediate Radius
Intermediate Radius / Minor Radius
Major Radius (nm)
4.0
3.5
3.0
2.5
2.0
1.5
1.0
600
500
400
300
200
100

b

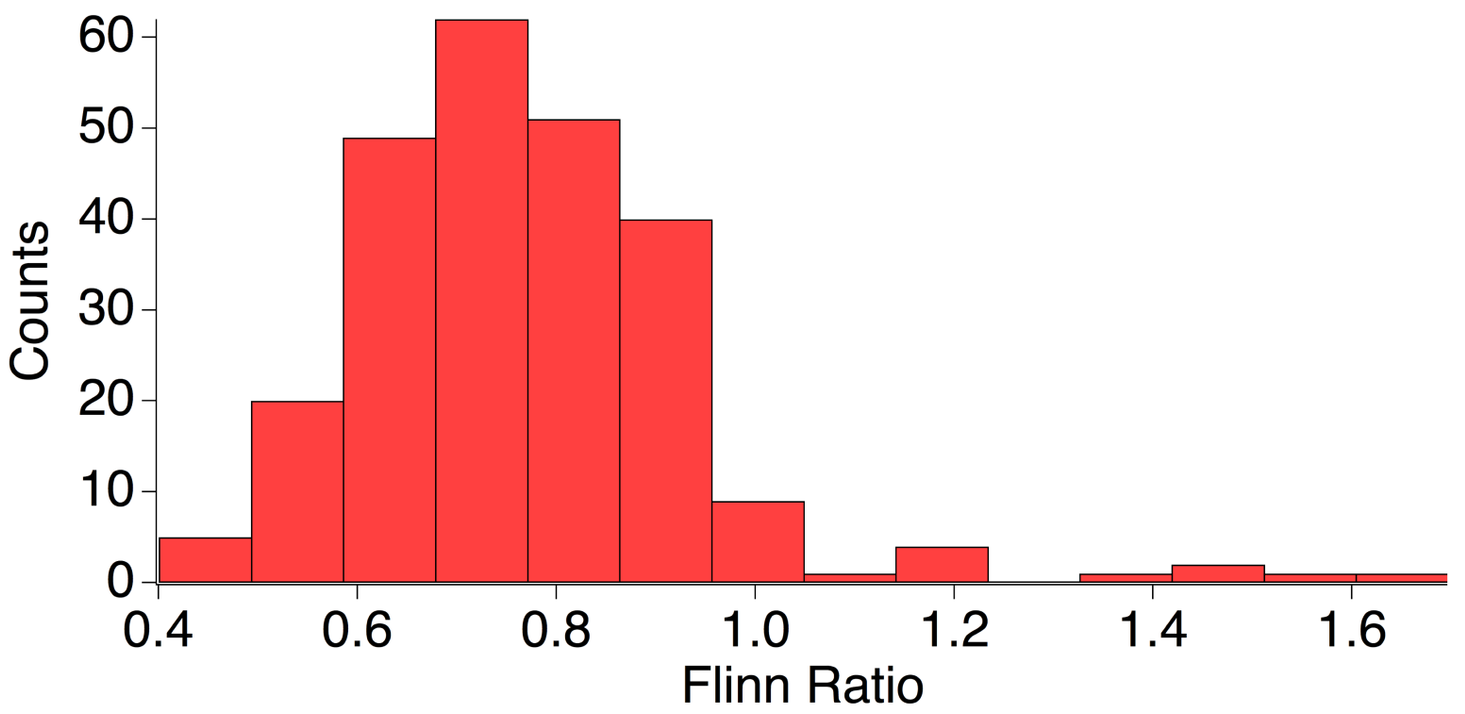
Counts
Flinn Ratio
60
50
40
30
20
10
0
0.4
0.6
0.8
1.0
1.2
1.4
1.6

Figure 7

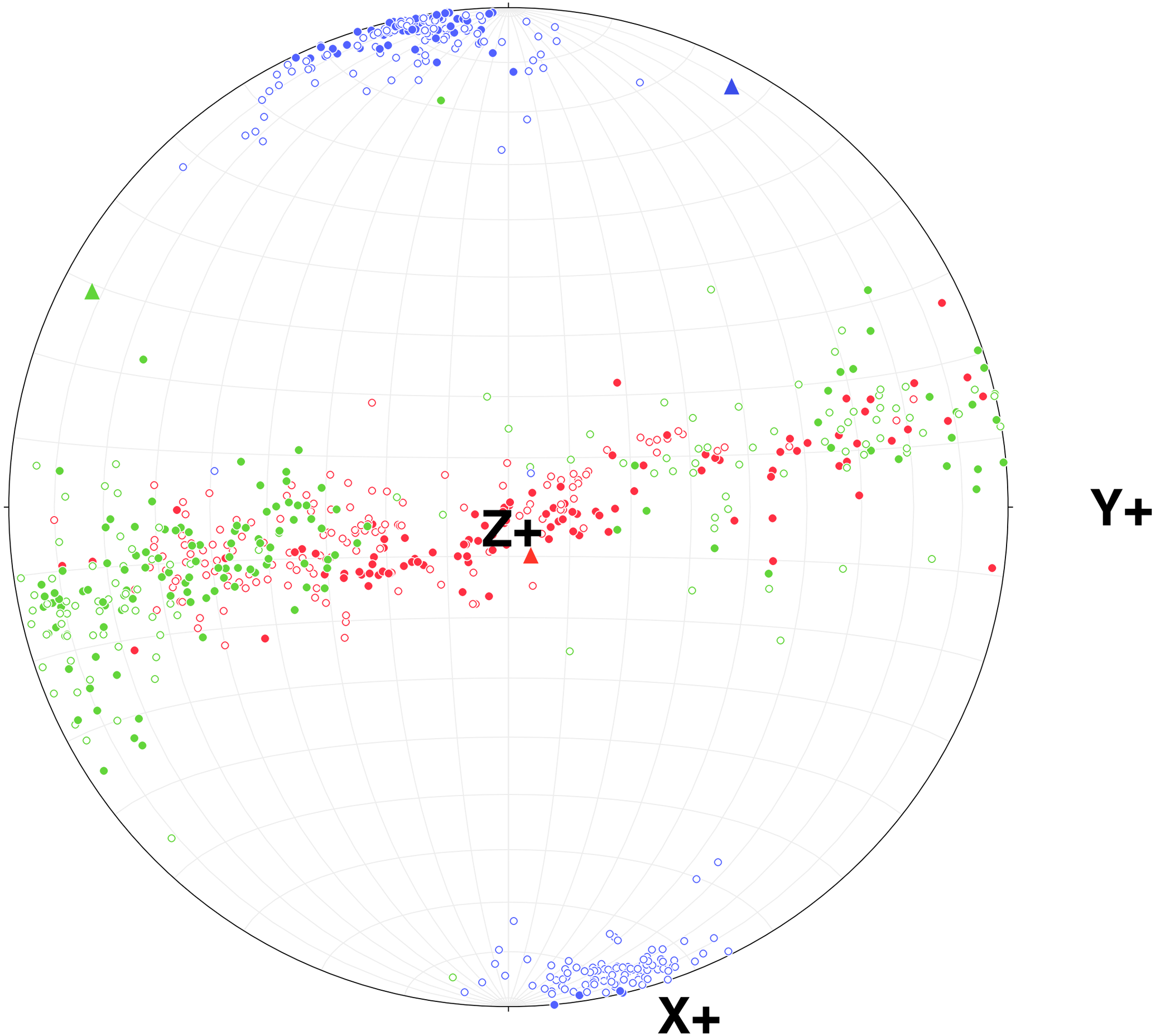

Figure 8

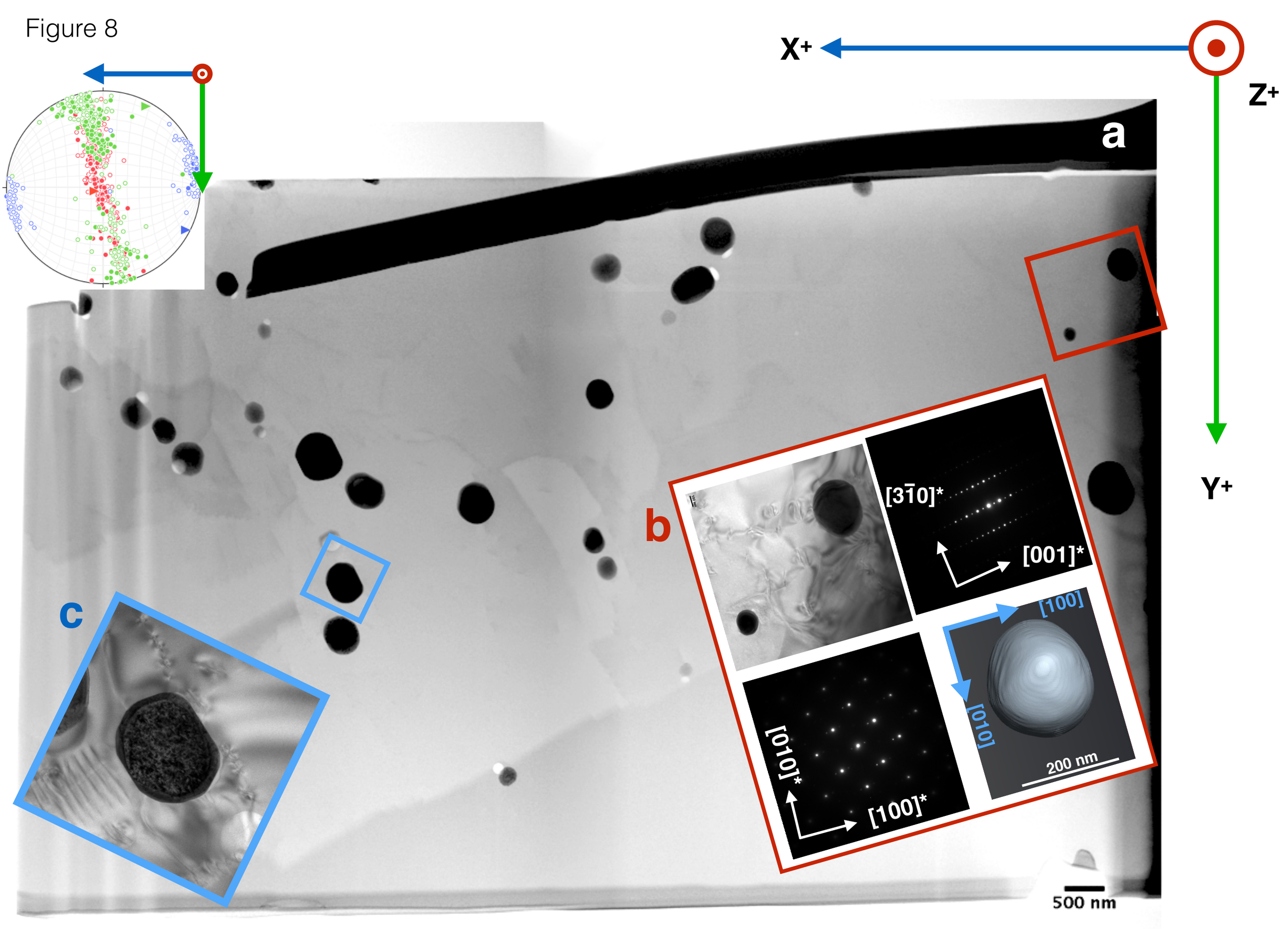

Figure 9

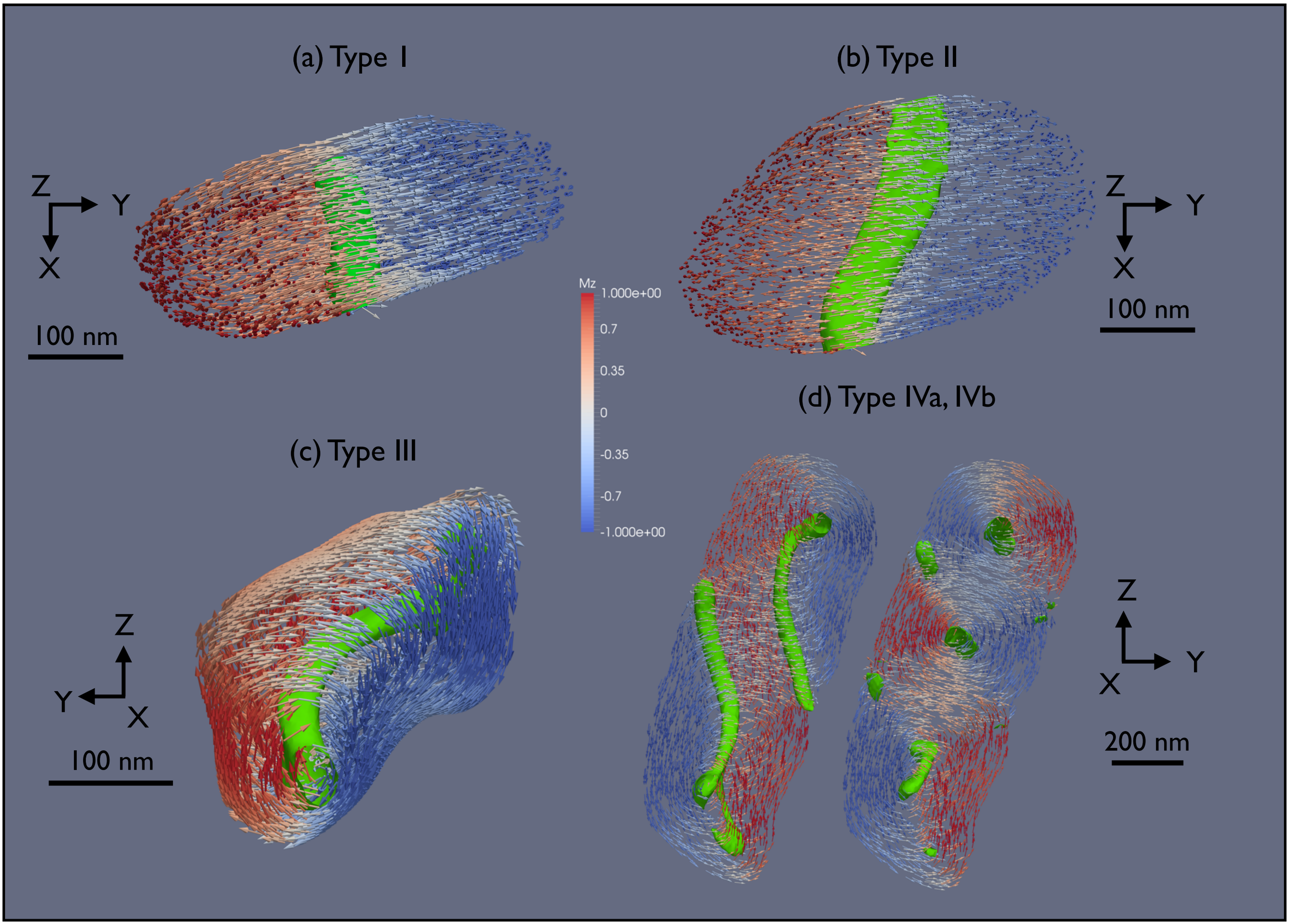
(a) Type I
Z
Y
X
100 nm
(b) Type II
Z
Y
X
100 nm
Mz
1.000e+00
0.7
0.35
0
-0.35
-0.7
-1.000e+00
(c) Type III
Z
Y
X
100 nm
(d) Type IVa, IVb
Z
Y
X
200 nm

Figure 10

(a) Particle 48

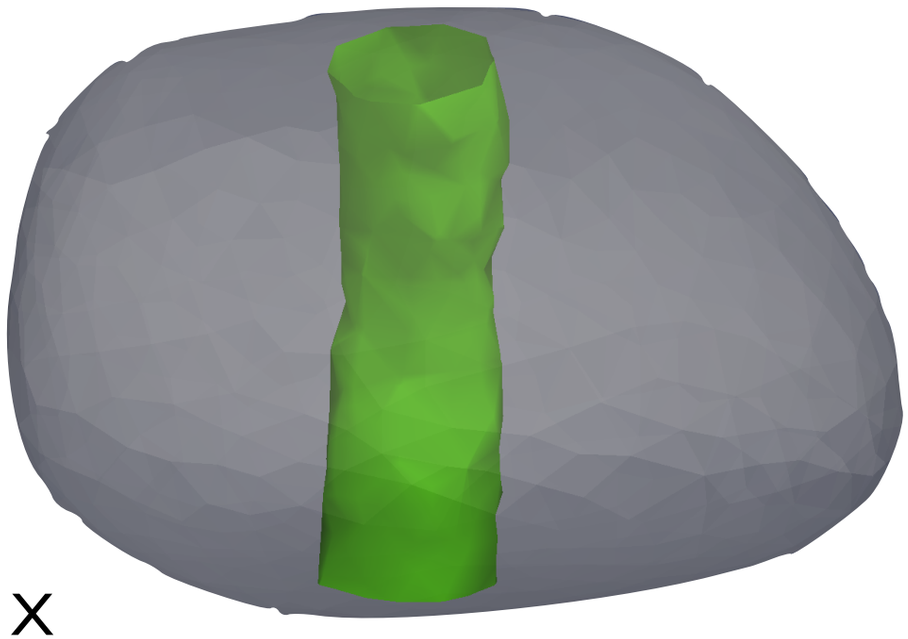

(b) Particle 165

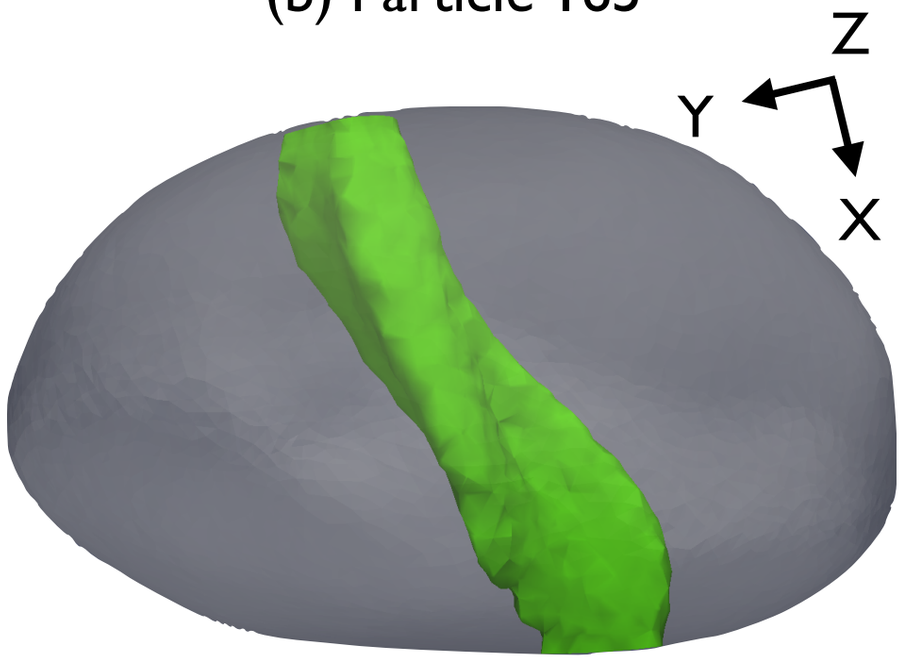

(c) Particle 8

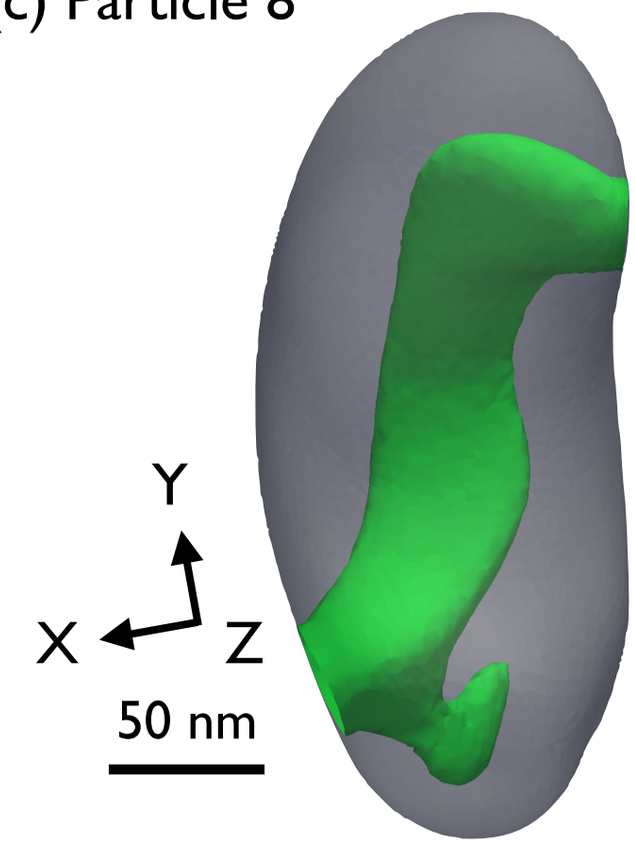

(d) Particle 75

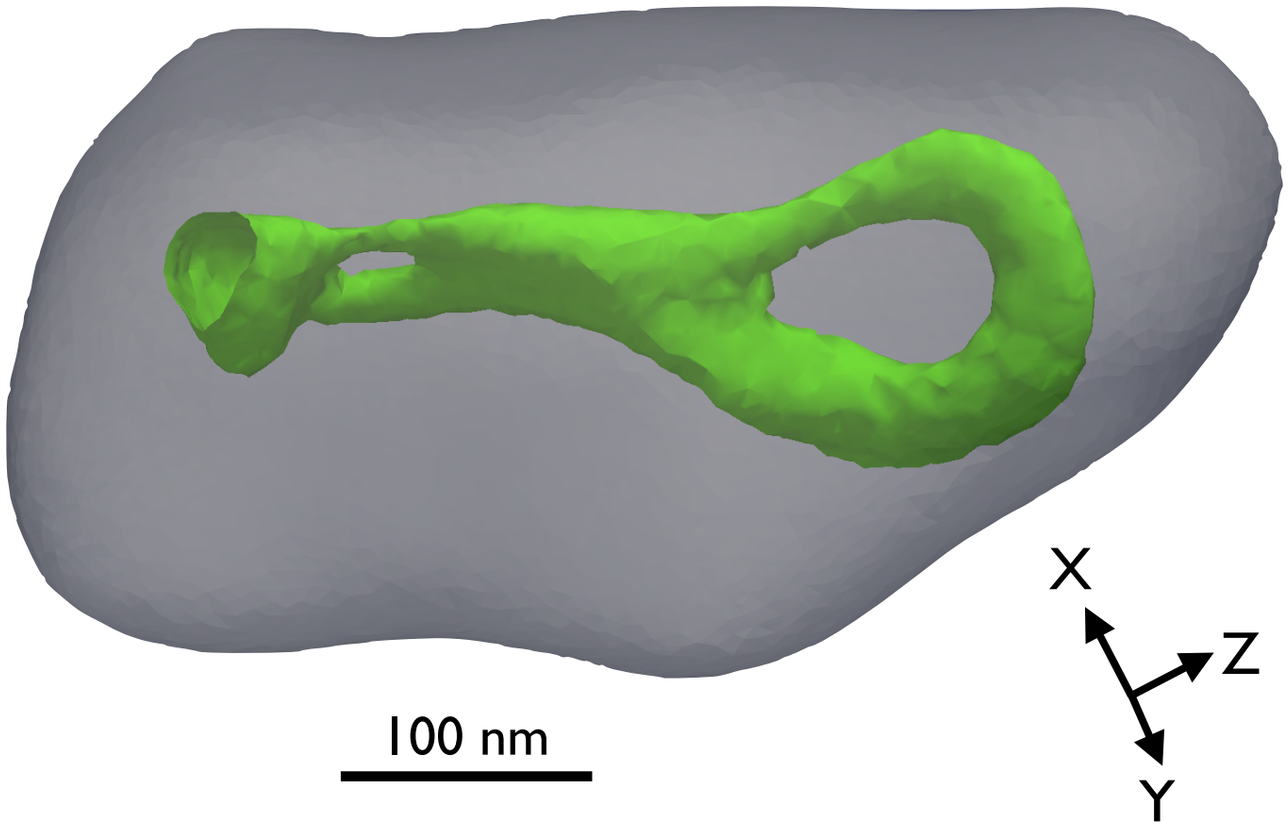

Figure 11

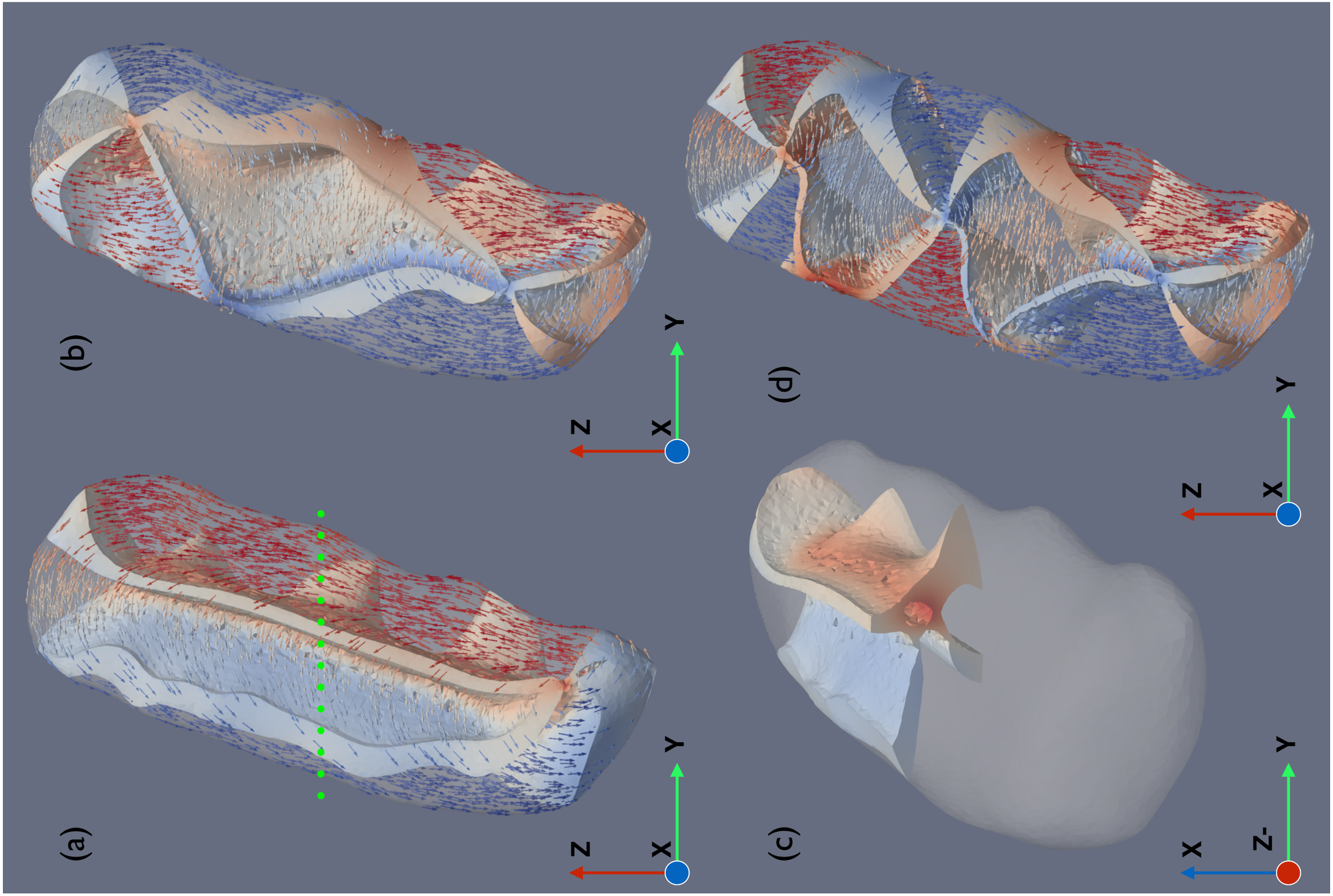

(a)

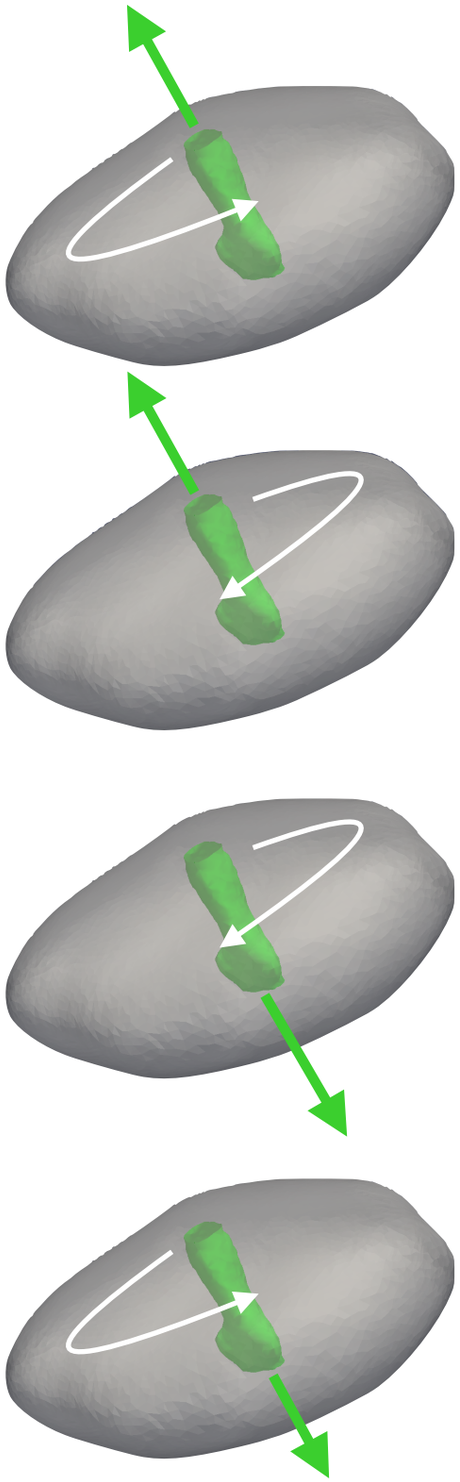

(b) Particle 364

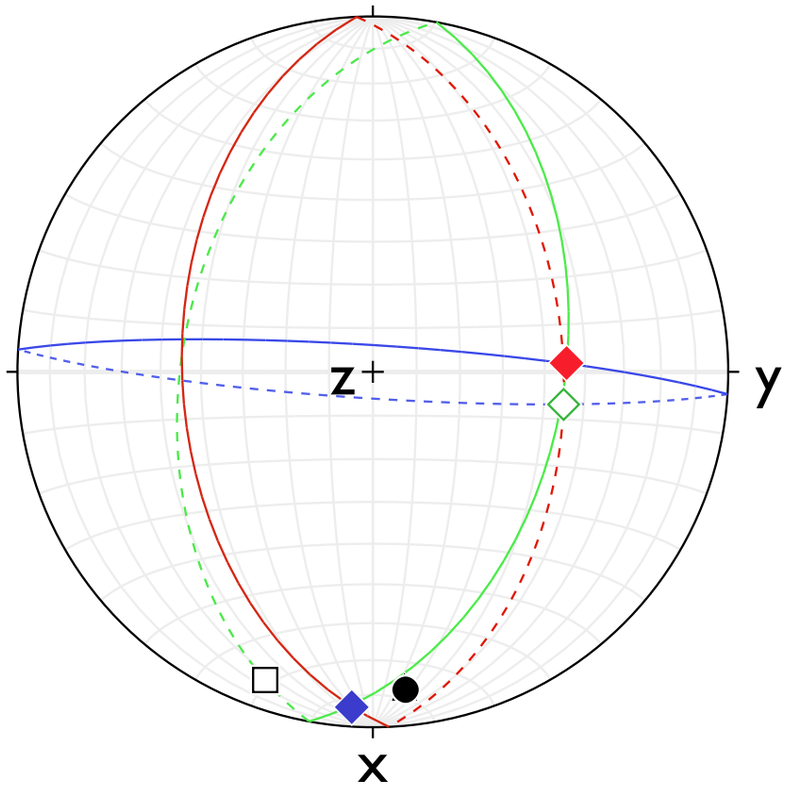

(c) Particle 155

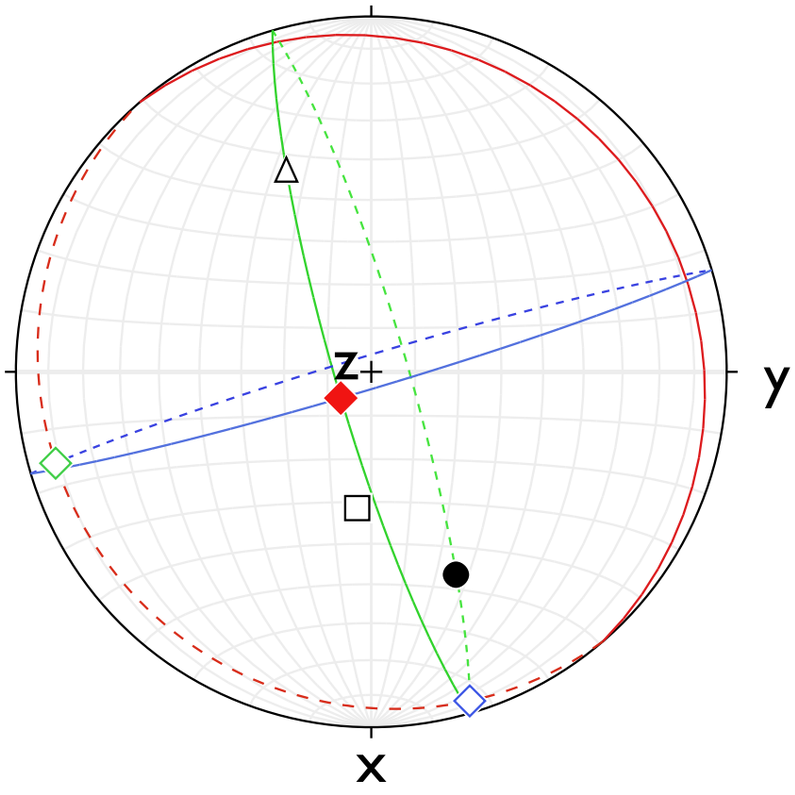

(d) Particle 165

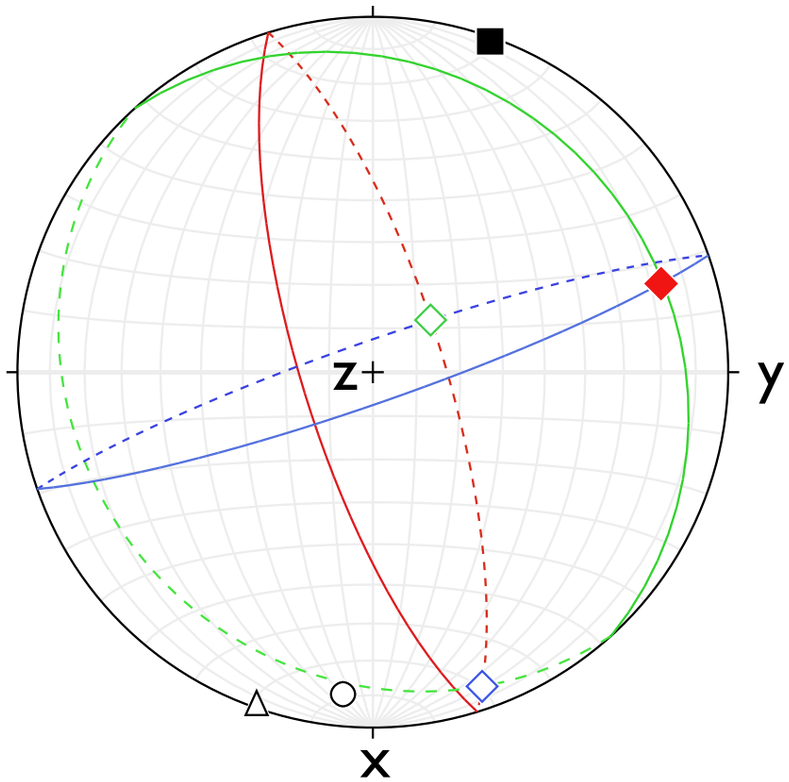

(e) Particle 8

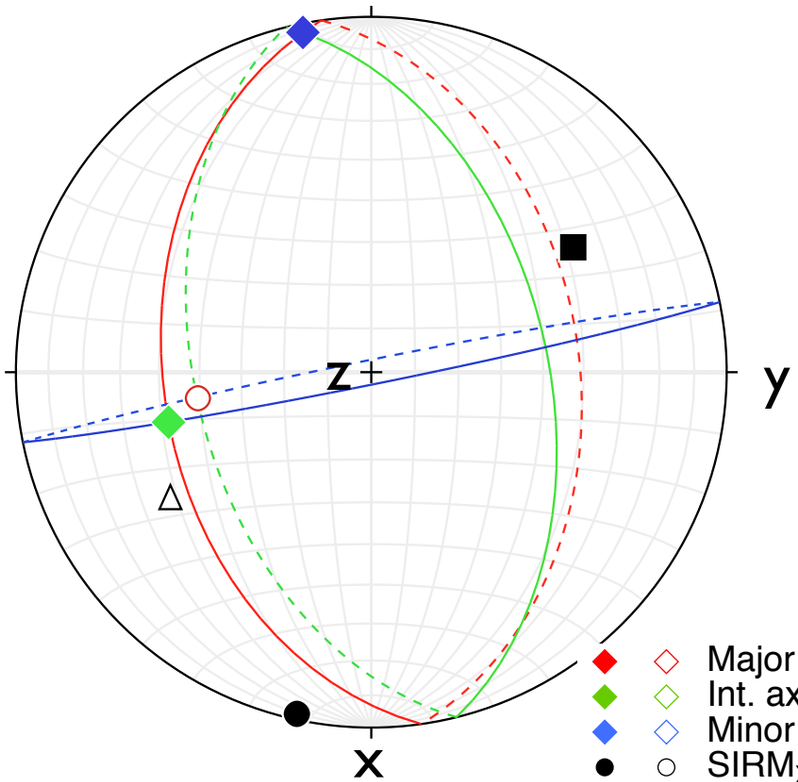

Major axis (down, up)
Int. axis (down, up)
Minor axis (down, up)
$SIRM_X$ (down, up)
$SIRM_Y$ (down, up)
$SIRM_Z$ (down, up)

Figure 12

Figure 13

(a) Particle 364 // X

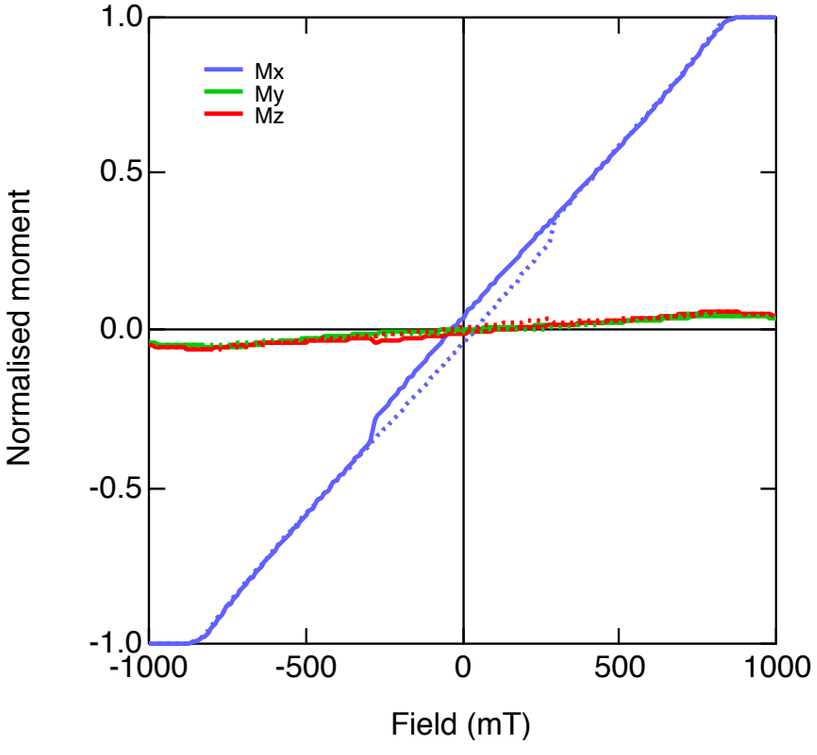

(b) Particle 48 // Y

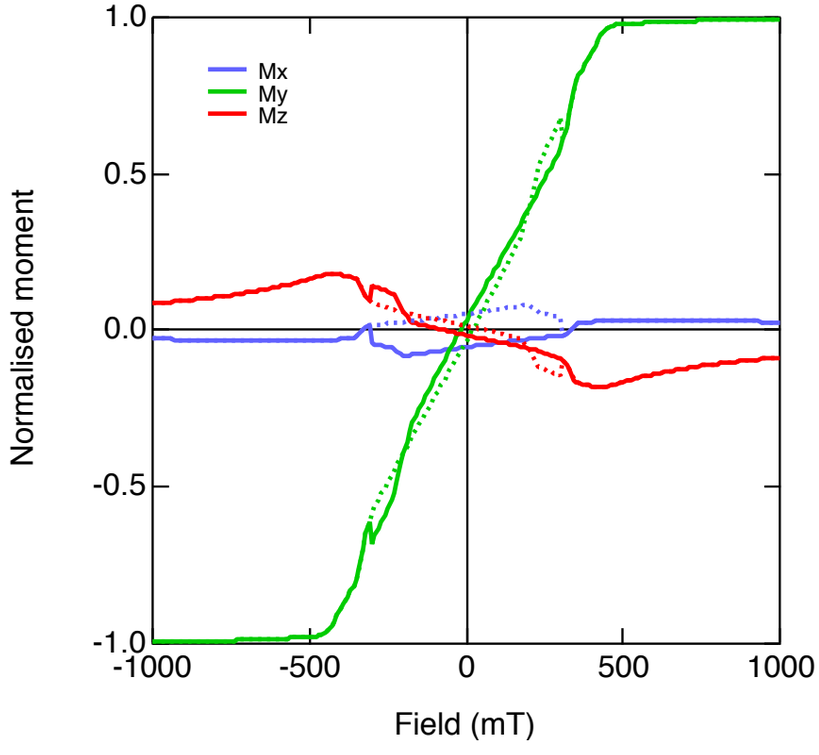

(c) Particle 48 // Z

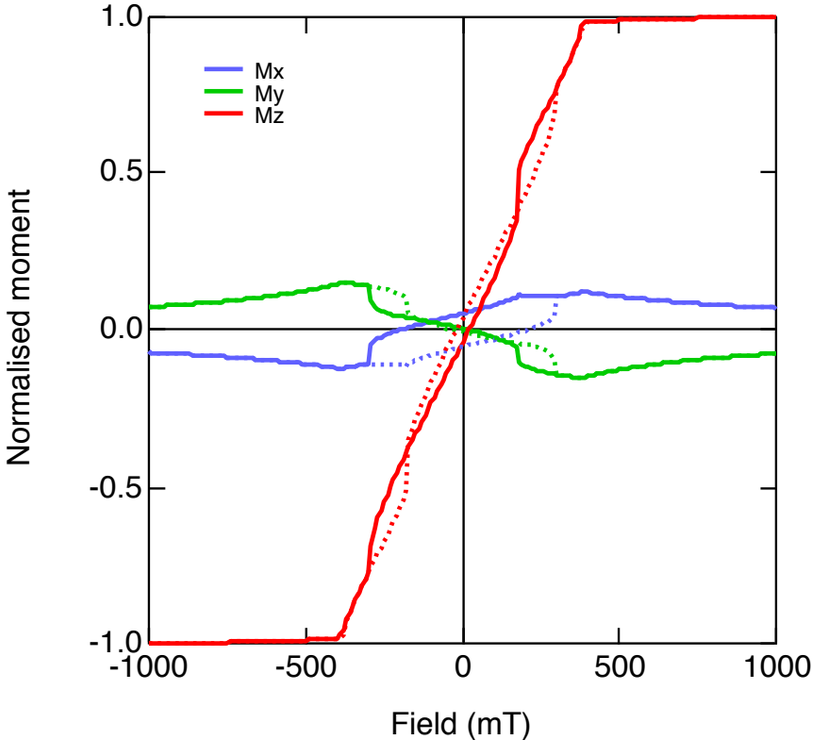

(d) Particle 233 // X

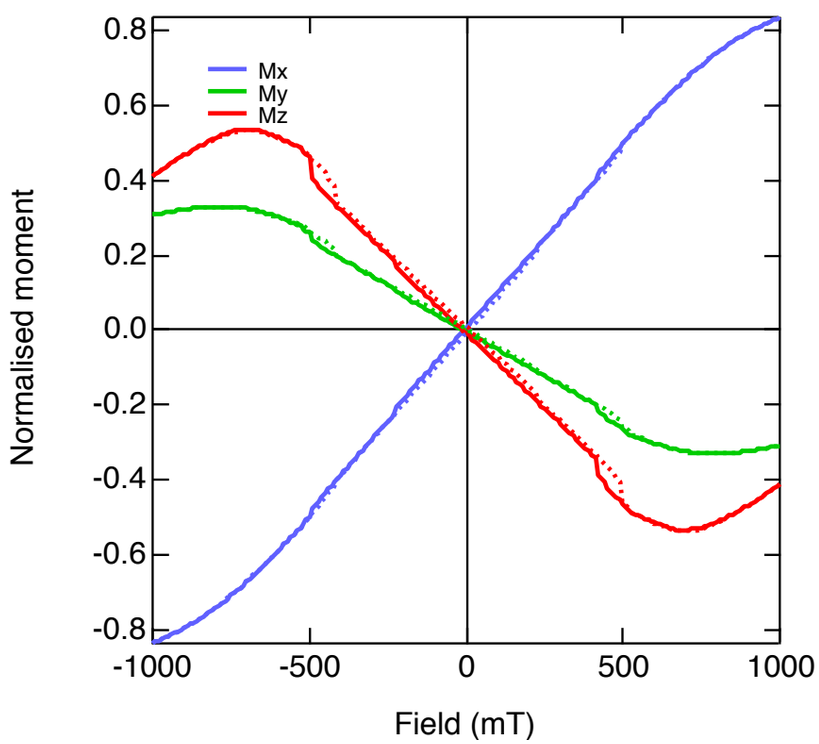

Figure 14